Czech
Technical
University
in Prague

F4

Faculty of Nuclear Science and Physical Engineering
Department of Solid State Engineering

Preparation and characterization of plasmonic nanostructures

Bc. Pavla Bérešová

Supervisor: doc. Ing. Ladislav Kalvoda, CSc.
June 2020

Acknowledgements

I would like to thank all the people who helped me during work on this thesis. First to my supervisor Ladislav Kalvoda for the corrections and Petr Kolenko for the support with planning the project. This work was supported by the Grant Agency of the Czech Technical University in Prague, grant No. SGS19/190/OHK4/3T/14 and the European exchange program Erasmus+. The work was done with the collaboration with the Leibniz-Institute for Photonic Technologies, where I carried out significant part of my work. Namely I thank Ondřej Stránik which supervised me during my stay in Jena. Thanks belongs as well to the department Nanobiophotonics and Microscopy, which I was assigned to, and all colleagues which helped me and introduced me to various techniques and measurements.

Declaration

I state that hereby presented work is result of my own effort and all used literature is listed. Prague, June 1, 2020

Abstract

Localised plasmon resonance and plasmon resonance are interesting phenomena possible to utilize for purpose of biosensing. Colloidal mask lithography techniques are convenient methods for creation of large areas of plasmonic nanostructures with sufficient stability and suitable plasmonic response for the biosensing applications. We have experimentally tested the methods of colloid mask, inverse colloid mask, hole-mask and AFM mask lithography. And we discuss the relevant parameters and procedural steps necessary to obtain biosensing suitable structure. Design of carbon monoxide sensor utilizing the nanodisc structure made by colloid lithography and change in myoglobin Q-band absorption spectra is proposed. The numerical model of the system together with protein measurements show that the change in the proteins Q-band is not sufficient to be reliably detected, despite the structures high sensitivity. The structures with sensitivity around 360 nm/RIU with limit of detection $\Delta n = 7 \cdot 10^{-5}$ RIU are nevertheless suitable platform for other aplications in biosensing.

Keywords: Plasmon resonance, Localised plasmon resonance, Colloid mask lithography, Hole-mask lithography, AFM mask lithography, CO sensing

Supervisor: doc. Ing. Ladislav Kalvoda, CSc.
CTU in Prague, Faculty of Nuclear Science and Physical Engineering

Abstrakt

Lokalizované povrchové plasmony a povrchové plasmony jsou fyzikální jevy vhodné pro využití pro biosenzoriku. Metody využívající koloidní litografie jsou jednoduché metody s nimiž jsme schopni vytvořit velké plochy plasmonických nanostruktur s dostatečnou stabilitou a plasmonickou odezvou pro tyto aplikace. Experimentálně jsme otestovali metody litografie koloidní masky, inverzní koloidní masky, masky s dírami a litografie pomocí AFM masky a diskutovali relevantní parametry důležité pro úspěšné dokončení struktur vhodných pro biosenzoriku. Byl navrhnut design senzoru na oxid uhelnatý využívající struktury nanodisků připravených pomocí litografie koloidní masky a změny Q-pásu v absorpčním spektru myoglobinu. Numerický model systému dohromady s naměřenými daty proteinu prokázal, že změna v absorpci Q-pásu není dostatečná aby byla spolehlivě detekovatelná, navzdory vysoké senzitivitě senzoru. Struktura se senzitivitou okolo 360 nm/RIU a limitem detekce změny indexu lomu $7 \cdot 10^{-5}$ RIU je však vhodnou platformou pro další aplikace v biosenzorice.

Klíčová slova: Plasmony, Lokalizované plasmony, litografie koloidní masky, litografie masky s dírami, litografie pomocí AFM masky

Překlad názvu: Příprava a charakterizace plasmonických nanostruktur

Contents

Introduction **1**

1 Theory **3**
1.1 Maxwell equations 3
1.1.1 Wave equation 4
1.1.2 Planar wave 5
1.2 Plasmons 6
1.2.1 Surface plasmon polariton 6
1.2.2 Single interface 7
1.2.3 Multilayer system 8
1.2.4 Transfer to localised surface plasmons 9
1.3 Localised surface plasmon resonance 10
1.3.1 Quasistatic approximation . . 11
1.3.2 Mie theory 13

2 Analysis and instrumentation **15**
2.1 Atomic force microscopy 15
2.2 Dark field microscopy 18
2.3 Spectral measurement 19
2.4 Microfluidics 20
2.5 Attenuated total reflection 20

3 Experimental methods and design **23**
3.1 Methods for structure preparation 23
3.1.1 Colloid mask lithography . . . 24
3.1.2 Inverse colloid mask lithography 24
3.1.3 Hole-mask litography 24
3.1.4 AFM mask lithography 26
3.1.5 Microarray spotting 27
3.2 Protein overview 27
3.3 Sensor design 29
3.4 Simulations 31

4 Results and discussion **33**
4.1 Simulations 33
4.2 Homogeneous assembly 33
4.2.1 Principle 33
4.2.2 Analysis 34
4.3 Gold deposition and thin film measurement 38
4.4 Inverse colloid mask lithography 41
4.5 Hole-mask lithography 43
4.6 AFM mask lithography 46
4.7 Colloid mask lithography 49
4.7.1 Stability of the structure 52
4.7.2 Simulation comparison 53
4.8 Microfluidic calibration measurement 55
4.9 Microarray plotting 57
4.10 Protein measurements 58
4.11 Protein simulations 59
4.11.1 Absorption and refraction indices 59
4.11.2 Extinction 61

Conclusions **63**

A Apendix **65**
A.1 Preparation of sample substrates 65
A.2 Protocol 68
A.3 Microarray plotting 69
A.4 Protein simulation 70
A.5 Summary of used equipment . . . 72

Bibliography **75**

Introduction

Metal thin films and nanoparticles can support collective resonant oscillations of their free electron. This phenomenon called surface plasmons for films and localized surface plasmon resonance for nanoparticles is leading to the absorption and scattering of light on optical frequencies [see 1, 2]. All of the plasmons are also very sensitive on the change of refractive index of surrounding media [see 3, 4], therefore they are used for sensor applications [see 5, 6]. The measurement of changes in the refractive index finds numerous applications in biosensing, where the variation of the refractive index is implied by the bonding of ligand on the sensor surface modified by protein. One of the first used methods is established on the Kretschmann setting for attenuated total reflection in plasmon resonance of the thin films [see 7]. The other possibility is using a transmission measurement for nanoparticles [see 8–13]. The nanoparticles show different plasmon resonance frequency depending on their various shape [see 14]. We can synthesize nanoparticles in the solution [see 15, 16], or we can fabricate the particles directly at the substrate by etching or deposition through the mask. A convenient method is an electron beam lithography [see 17, 18], which is very precise but requires the cleanroom environment and it is time and money consuming. Therefore in our interest will be the less demanding and cheaper methods not requiring cleanroom environment. Those are the mask methods. In these methods, we can create nanostructures of various shapes; from nanotriangles [see 19–21], nanodiscs [see 22] up to complicated patterns [see 23].

This thesis focuses primarily on the colloid methods such as colloid mask lithography and hole-mask lithography. We also introduce new mask method called AFM mask lithography derived from a combination of standard AFM lithography and hole-mask lithography principle. Additionally, this work handles the problem of carbon monoxide sensing by modeling and designing of a plasmonic sensor in tandem with a protein. The sensor is based on the structure of golden nanodisc together with horse myoglobin which bonds the gas. The emphasis is put on the stability and sensitivity of the resulting sensor and its versatility and possibility to be used as well in other biosensing measurements.

Chapter 1

Theory

To fully understand how and why we use plasmonic nanostructures as an optical based sensor, we need to look at the problem of optical properties of metal in scales raging from thin layer systems [see 24], up to systems with nanoparticles [see 25–27]. For this means, we start with specifying the system properties and boundary conditions and understanding general Maxwell equations [taken from 28] to obtain dispersion relations, absorption coefficients and other important properties of the system.

1.1 Maxwell equations

As for any other optical system, for describing plasmons, we need to start from the very beginning; the Maxwell equations. They give us vital connection in between the electric ($\mathbf{E}$) and magnetic ($\mathbf{H}$) fields, dielectric displacement ($\mathbf{D}$) and magnetic induction ($\mathbf{B}$) as well as describing the general problem of electromagnetic waves (EM waves) propagating in a medium.

$$\begin{aligned} \nabla \times \mathbf{E} &= \frac{\partial \mathbf{B}}{\partial t} & \nabla \times \mathbf{H} &= \frac{\partial \mathbf{D}}{\partial t} + \mathbf{j}_{ext} \\ \nabla \cdot \mathbf{D} &= \rho_{ext} & \nabla \cdot \mathbf{B} &= 0, \end{aligned} \tag{1.1}$$

Where ρ_{ext} and $\mathbf{j}_{ext}$ are external charge and current densities. Together with the response of a medium ρ and $\mathbf{j}$ they give the total charge and current densities in the system. The electric displacement is further linked with the electric field via polarization ($\mathbf{P}$) and the magnetic field is connected to the induction via magnetization ($\mathbf{M}$). The system is also governed by the material constitutive relations for a linear, homogeneous and isotropic medium.

$$\begin{aligned} \mathbf{D} &= \varepsilon_0 \mathbf{E} + \mathbf{P} & \mathbf{j} &= \sigma \mathbf{E}, \\ \mathbf{H} &= \frac{\mathbf{B}}{\mu_0} - \mathbf{M} & \mathbf{B} &= \mu_0 \mu_r \mathbf{H}, \\ & & \mathbf{D} &= \varepsilon_0 \varepsilon_r \mathbf{E}, \end{aligned} \tag{1.2}$$

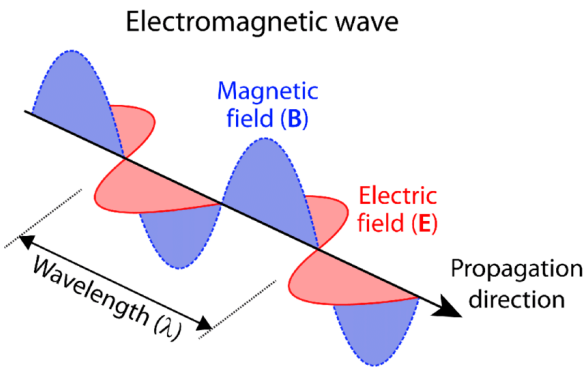

Figure 1.1: The visualization of a harmonic electromagnetic wave, the electric field $\mathbf{E}$ and magnetic field $\mathbf{H}$ are perpendicular [taken from 29].

where μ_0[1], ε_0[2], μ_r, ε_r and σ are respectively the vacuum permeability,vacuum permittivity, relative permeability, permittivity and conductivity. We also must note that we consider $\mu_r = 1$ for the non magnetic medium as we are going to use gold in our nanostructures. Utilizing all these properties changes the Maxwell equation to the form

$$\nabla \times \mathbf{E} = -\mu_0 \frac{\partial \mathbf{H}}{\partial t} \qquad \nabla \times \mathbf{H} = \varepsilon_0 \varepsilon_r \frac{\partial \mathbf{E}}{\partial t} + \sigma \mathbf{E}$$
$$\nabla \cdot (\varepsilon_0 \varepsilon_\mathrm{r} \mathbf{E}) = 0 \qquad \nabla \cdot \mathbf{H} = 0. \tag{1.3}$$

1.1.1 Wave equation

Another step in the description of the plasmon is the wave equation. In order to look how the EM wave propagates we need to derive the wave equation and make an assumption of the wave form. Using the curl operator and mathematical identity $\nabla \times \nabla \times \mathbf{E} = \nabla(\nabla \cdot \mathbf{E}) - \nabla^2 \mathbf{E}$ we obtain the wave equation. The wave equation for $\mathbf{E}$ is then

$$\nabla^2 \mathbf{E} = \mu_0 \varepsilon_0 \varepsilon_r \frac{\partial^2 \mathbf{E}}{\partial t^2} + \mu_0 \sigma \frac{\partial \mathbf{E}}{\partial t}. \tag{1.4}$$

We assume a harmonic solution in the wave form $\mathbf{E}\,(r,t) = \mathbf{E}\,(r)\,\mathrm{e}^{-\mathrm{i}\omega t}$ where ω is angular frequency. The visualization of such a wave can be seen in fig. 1.1. Separability of the $\mathbf{E}(r,t)$ spacial and time part, leads us to the form

$$\nabla^2 \mathbf{E} + \omega^2 \left(\mu_0 \varepsilon_0 \varepsilon_r + \mathrm{i} \frac{\sigma \mu_0}{\omega} \right) \mathbf{E} = 0. \tag{1.5}$$

[1] $\mu_0 = 4\pi \times 10^{-7}\mathrm{H/m}$

[2] $\varepsilon_0 = \dfrac{1}{36\pi} \times 10^{-12}\mathrm{F/m}$

Introducing some basic relation for vacuum $\varepsilon_0\mu_0 = \frac{1}{c^2}$ and the wave vector $k_0 = \frac{\omega}{c}$ we can define the complex permittivity for the lossy medium

$$\hat{\varepsilon}_r = \varepsilon_r + \mathrm{i}\frac{\sigma}{\varepsilon_0\omega} \tag{1.6}$$

which is describing additionally the losses of the system. To simplify the notation we will continue using ε_r as a notation for permittivity of the system[3]. We can rewrite the wave equation into the the form called Helmholtz wave equations

$$\begin{aligned} \nabla^2\mathbf{E} + k_0^2\varepsilon_r\mathbf{E} = 0. \\ \nabla^2\mathbf{H} + k_0^2\varepsilon_r\mathbf{H} = 0. \end{aligned} \tag{1.7}$$

1.1.2 Planar wave

Because our goal is to describe surface plasmons which occur on thin film interfaces, we first need to specify the propagation of light in such a planar system. The geometrical representation of our system in the first approximation is a plane in xy with a wave propagating solely in x-direction. Therefore we have one dimensional propagation where permittivity depends only on one spatial coordinate $\varepsilon_r = \varepsilon_r(z)$. Also for this geometry the relation for the electric field can now be simplified to $\mathbf{E}(\mathbf{r}) = \mathbf{E}(z)e^{\mathrm{i}\beta x}$ where β is complex parameter denoted as the propagation constant $\beta = k_x$. It corresponds to the component of the wave vector in x-direction along which the wave propagates. Inserting these in the wave equation we obtain

$$\frac{\partial^2\mathbf{E}(z)}{\partial z^2} + \left(k_0^2\varepsilon_r - \beta^2\right)\mathbf{E} = 0. \tag{1.8}$$

The same relation naturally holds for the magnetic field $\mathbf{H}$.

We can look at the components of the wave equation and the Maxwell curl equations and divide them into two independent sets of equations. The first includes only the field components $\mathbf{E}_x$, $\mathbf{E}_z$ and $\mathbf{H}_y$ which are nonzero and the corresponding waves are called transversal magnetic (TM). The transversal electric (TE)[4] wave has remaining components $\mathbf{H}_x$, $\mathbf{H}_z$ a $\mathbf{E}_y$

$$\begin{aligned} \mathbf{E}_x &= -\mathrm{i}\frac{1}{\omega\varepsilon_0\varepsilon_r}\frac{\partial\mathbf{H}_y}{\partial z} & \mathbf{H}_x &= -\mathrm{i}\frac{1}{\omega\mu_0}\frac{\partial\mathbf{E}_y}{\partial z} \\ \mathbf{E}_z &= -\frac{\beta}{\omega\varepsilon_0\varepsilon_r}\mathbf{H}_y & \mathbf{H}_z &= -\frac{\beta}{\omega\mu_0}\mathbf{E}_y \\ \frac{\partial^2\mathbf{H}_y}{\partial z^2} &+ \left(k_0^2\varepsilon_r - \beta^2\right)\mathbf{H}_y = 0 & \frac{\partial^2\mathbf{E}_y}{\partial z^2} &+ \left(k_0^2\varepsilon_r - \beta^2\right)\mathbf{E}_y = 0. \end{aligned} \tag{1.9}$$

[3] From now on the permittivity is a complex value.

[4] There is also other way of noting TM and TE wave. The notation originates from German where the TM wave is corresponding to polarisation 'p' ('parallel') and TE wave corresponding to polarisation 's'('senkrecht' meaning perpendicular).

We can also visualize what TE wave has the electric field non-zero value only in the xy plane, whereas the TM wave can have non-zero component in the z direction (can have effect environment not only in the the xy plane).

So far we are looking in a general way on the Maxwell equations, making small assumptions to specify them. This will allow us to effectively explain plasmons without long auxiliary calculations.

1.2 Plasmons

The general characteristics of metals are determined by the presence of free electrons. Plasmons are generally described as quantized oscillations of the electron gas (respectively charge density oscillations). According to the Drude-Lorentz model utilizing the dipole oscillator approximation for free electrons with negligible damping we can write:

$$\varepsilon(\omega) = 1 - \frac{\omega_p^2}{\omega^2} \tag{1.10}$$

where ω_p is known as the plasma frequency[5]. This frequency is connected to the edge of the ultra-violet transparency of metals and has an important role in describing bulk and surface plasmons.

The dispersion relation for the bulk plasmon then can be derived via the Maxwell equation for the electric field $\mathbf{E}$ and current density $\mathbf{j}$. Subsequently the equations for separately the transversal and longitudinal plasmon modes and wave like solutions $\mathbf{E} = \mathrm{e}^{\mathrm{i}(kr-\omega t)}$ lead us to the dispersion relation $c^2k^2 = \omega^2 - \omega_p^2$ for transversal and $\omega = \omega_p$ for the longitudinal wave. We can see that the metal characteristics of plasmons are limited by the condition $\omega \geq \omega_p$; under the plasma frequency the incoming wave is reflected by the plasma. The relation is depicted in fig. 1.3 on page 8 together with the surface plasmon polariton dispersion relation and dispersion relation of light in vacuum.

1.2.1 Surface plasmon polariton

Surface plasmon polaritons (SPP) are a type of plasmon bound to the interface between a metal and an insulator. They are quasiparticles representing collective oscillation of free electrons in the metal coupled with the exciting electromagnetic wave. SPP are characterized with evanescent decay in perpendicular direction to the surface. For describing such system we will use two different approximations, single interface and the multilayer system. We will also neglect the possible polarization and magnetization components of surface plasmon polaritons, to simplify the thought process.

[5] $\omega_p = \dfrac{Ne^2}{\varepsilon_0 m}$, where N - number of an electron, e - charge of an electron, m - mass of an electron.

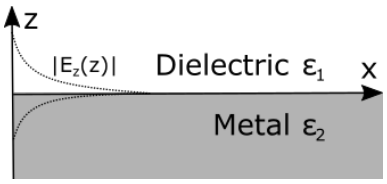

Figure 1.2: Schema of a metal-dielectric interface in between the dielectric and the metal with indicated evanescent decay of the field in the out of plane direction.

1.2.2 Single interface

The simplest geometry on which the SPP can be described is a single interface between a metal and an insulator (fig. 1.2). The insulator is a dielectric with positive real dielectric constant ε_1 in the half space $z > 0$. The metal in the half space $z < 0$ is conducting and characterized with the permittivity $\varepsilon_2(\omega)$. The metal dielectric function has a negative real part $\mathrm{Re}(\varepsilon_2) < 0$, whereas the dielectric constant $\varepsilon_1$is alwazs positive. The sign difference in between the real parts of the permittivities is the vital characteristic of the system allowing the surface plasmon polaritons to exist [30, 31].

Now we implement the continuity conditions of the interface to the equations of the planar wave at the interface 1.1.2. For the TM wave, we get the following relation between k_{z1}, k_{z2} (components of k_z belonging to the different media) and permittivities

$$\frac{k_{z1}}{k_{z2}} = -\frac{\varepsilon_1}{\varepsilon_2}. \tag{1.11}$$

The fraction of k_{z1} and k_{z2} is positive, therefore the Maxwell equations lead us to the requirement of opposite signs between permittivities ε_1 and ε_2. This condition is exactly fulfilled by the metal/dielectric interface as mentioned above. From the Helmholtz equation, expressing H_y, we can acquire further conditions, which then lead us to the dispersion relation for SPP confined at the metal-dielectric interface

$$\beta = k_0\sqrt{\frac{\varepsilon_1\varepsilon_2}{\varepsilon_1 + \varepsilon_2}}. \tag{1.12}$$

Analogically we could proceed with the TE wave. The final condition would depend on the scaling constant of the field A_i which originates from the integration[6],

$$A_1\left(k_{z1} + k_{z2}\right) = 0. \tag{1.13}$$

The values of $k_{z1,2}$ are always positive, therefore the only solution is $A_1 = 0$ and equivalently $A_2 = 0$. This means that there is no propagating wave for the TE modes at the interface. The SPP exists only for the TM wave.

For large wave vectors $k_x \to \infty$, the SPP frequency aproaches the characteristic surface plasmon frequency

$$\omega_{sp} = \frac{\omega_p}{\sqrt{1 + \varepsilon_1}}. \tag{1.14}$$

[6]The constant A_i also represents the amplitude of the corresponding wave.

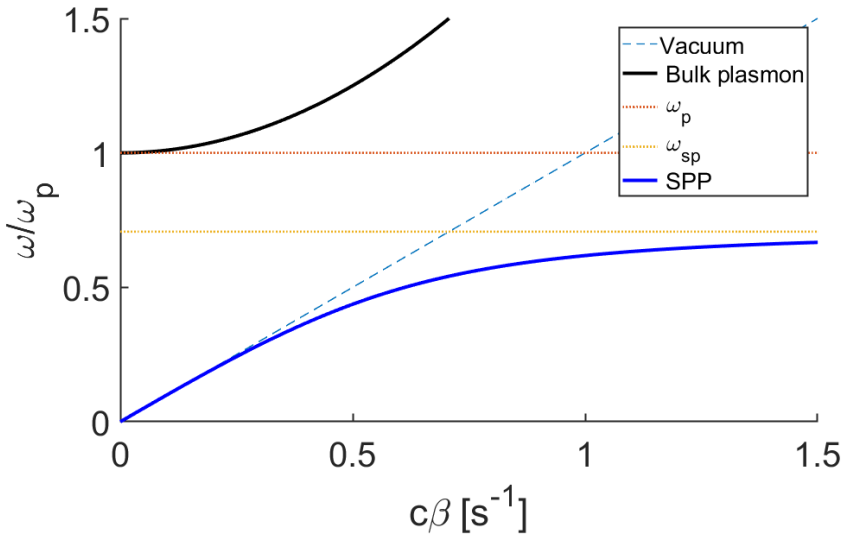

Figure 1.3: Dispersion relation for bulk plasmon (black), light in vacuum (dash) and surface plasmon polariton - theoretical curve (blue) uses the Drude-Lorentz model.

The asymptotic values of ω_{sp} and ω_p for $k = 0$ and their relation to the dispersion relations of bulk plasmons, light in vacuum and surface plasmon polariton are shown in fig. 1.3. In the calculation of the theoretical curve of SPP, the metal dielectric function ε_2 was calculated from the Drude-Lorentz model (eq. 1.10).

1.2.3 Multilayer system

Although the single interface system gave us an easy approximation of behaviour of SPP, the model is still far from reality. To show that better approximations of the system do not lead to qualitatively different results, we can look on the propagation of TM modes from a perspective of sandwich multilayer systems as in [24, 32, 33]. This requires extensive calculations, so we will only present the results. In applications, these systems are divided in to two categories, metal/insulator/metal (MIM) structures and insulator/metal/insulator (IMI) structures (figure 1.4), and are realized mostly in form of rectangular waveguides.

The multilayer system is generally governed with the same Maxwell wave equations. Due to the more complicated geometry of the system, more boundary conditions needs to be fulfilled. Therefore the solutions will split into an odd and an even branch (fig. 1.5) depending on the overall parity of the field. The resulting curve takes form of tanh function. For example the odd branch:

$$\tanh(k_z^1 a) = -\frac{k_z^2 \varepsilon_1}{k_z^1 \varepsilon_2}. \tag{1.15}$$

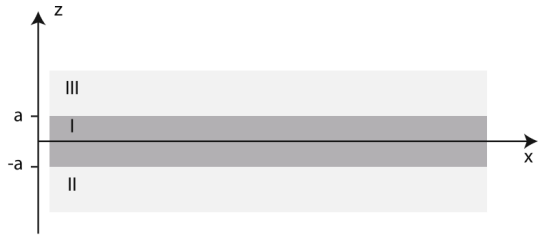

Figure 1.4: Scheme of a multilayer system supporting SPP. We can distinguish in between MIM (II and III metal, I dielectrics) and IMI (I metal, II and III dielectric) structures.

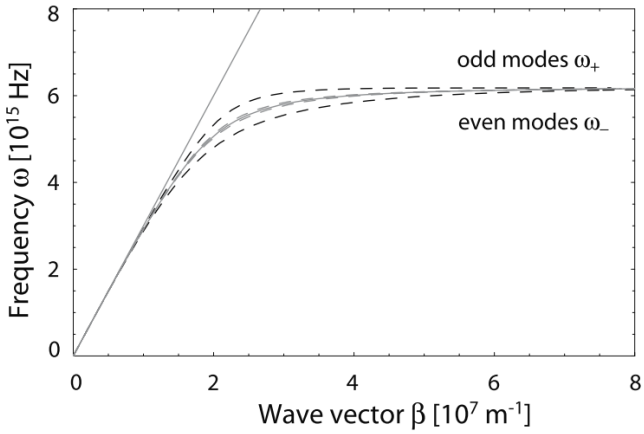

Figure 1.5: Comparison of the calculated dispersion relations resulting from the different approximations for IMI structure with central silver layer. Dashed lines represent multilayer system (grey for 100 nm thick layer and black for 50 nm thick layer) while the solid line represents the single interface approximation [taken from 24].

1.2.4 Transfer to localised surface plasmons

Now we will finalize the picture of the surface plasmon polaritons and make a thought transfer to localised surface plasmons. So far we described a propagating wave in the film. This description can be visualized as a change of charge on the metal/dielectric interface (fig. 1.6). The description of SPP is based on planar infinite media, but the localised plasmons are observed on small nanoparticles of various shapes, therefore a simplest model we can use is a sphere. The theory made by Sun and Khurgin [see 34] suggest approaching the sphere as a curved interface. This way the surface plasmon gets bounded and manifests in form of mode oscillations; describing the mode frequency ω_l of the mode l

$$\omega_l = \omega_p \sqrt{\frac{l}{l + (l+1)\,\varepsilon_1}} \tag{1.16}$$

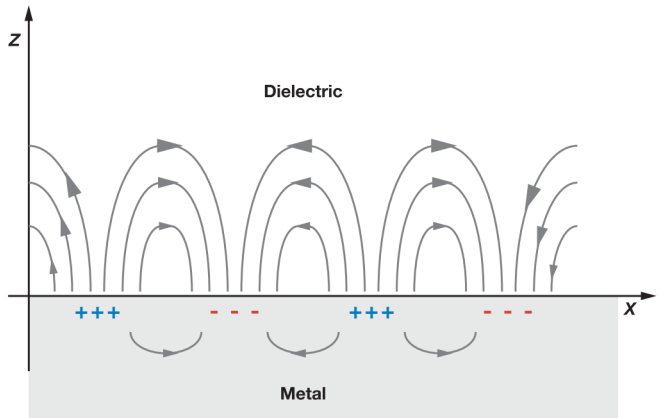

Figure 1.6: Representation of the surface plasmon polariton as an oscillation of free electrons together with the evanescent EM field within a metal/dielectric interface [taken from 9].

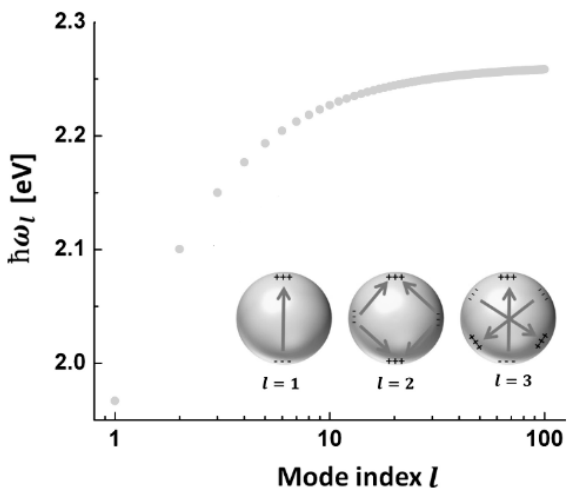

Figure 1.7: The dependency of the energy $\omega_l \hbar$ on the oscillation mode l, the imprint shows a scheme of the first three modes [modified from 34].

where the ε_1 refers to the permittivity of the dielectric as it was in the description of surface plasmons. This formula gives us a relation for frequency dependent on the mode number (fig. 1.7). The graph also shows the visualization of the first three modes. As the mode number increases the frequency ω_l approaches the limit value of a ω_{sp}. This result provides a connection between phenomena occurring on thin films and in nanoparticles.

1.3 Localised surface plasmon resonance

As we moved to the description of the localized plasmon surface resonance (LSPR), we noted that the situation is a bit different from surface plasmons. The phenomenon is observed on single metallic nanoparticles consisting

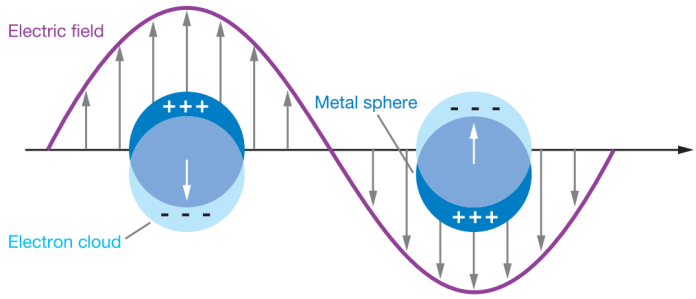

Figure 1.8: Oscillation of inbound electrons in a plasmonic nanoparticle [taken from 9].

of a plasmonic active material. The LSPR is not propagating because its bounded to the nanoparticle small volume. The mode approach can be described as a collective oscillation of free electrons in the nanoparticle. For small particles under 10 nm, where the dipole oscillations contribute the most [see 35, 36] we can depict the oscillations as in fig. 1.8. Such an model idea will help us to interpret the results of the analytical and the numerical solutions of the EM field behaviour in the nanoparticles and their surrounding. The more complicated approaches will then give us the qualitative results.

1.3.1 Quasistatic approximation

One of possible solution is derived for small spherical particles with radius $a \ll \lambda$. In this case the change of field through the particle volume is negligible, so we can search at the excitation field as being constant in space. We can therefore first look for the static field solutions [as in 37] and add the time dependence later. Such an approximation allows us to solve the Laplace equation and derive the form of the EM wave inside and outside the particle.

Looking at a particle characterized with the dielectric function $\varepsilon(\omega)$ surrounded by an isotropic non-absorbing medium with the dielectric constant ε_m, which is located in the static electric field $\mathbf{E} = E_0\mathbf{z}$, we obtain the following fields inside and outside of the particle:

$$\mathbf{E}_{\text{in}} = -\frac{3\varepsilon_m}{\varepsilon + 2\varepsilon_m}\mathbf{E}_0 \tag{1.17a}$$

$$\mathbf{E}_{\text{out}} = -\mathbf{E}_0 + \frac{3\mathbf{r}(\mathbf{rp} - \mathbf{p})}{4\pi\varepsilon_0\varepsilon_m r^5}, \tag{1.17b}$$

where $\mathbf{p}$ is the induced total dipole moment. The polarizability of the particle is then given as

$$\alpha = 4\pi a^3 \frac{\varepsilon - \varepsilon_m}{\varepsilon + 2\varepsilon_m}. \tag{1.18}$$

The resonance frequency is given by the so called Fröhlich condition

$$\Re[\varepsilon(\omega)] = -2\varepsilon_m \tag{1.19}$$

which shows its importance for metallic particles with the corresponding frequency

$$\omega_0 = \frac{\omega_p}{\sqrt{3}}. \tag{1.20}$$

On this frequency it is possible to experience LSP and therefore measure small changes of the refractive index ε_m.

Proceeding with the quasistatic approximation we use dipole approximation for the small sphere. Now for the time-dependent illuminating wave $\mathbf{E}(\mathbf{r}, t) = \mathbf{E}_0 e^{-\mathrm{i}\omega t}$. The field induces a dipole moment $\mathbf{p}(t) = \varepsilon_0 \varepsilon_m \alpha \mathbf{E}_0 e^{-\mathrm{i}\omega t}$ with the polarizability resulting from the static approximation (eq. 1.18). The scattering of the plane wave can be written in a form of dipole radiation

$$\mathbf{E}(t) = \frac{1}{4\pi\varepsilon_0\varepsilon_m}\mathbf{E}_{dip} e^{-\mathrm{i}\omega t}, \tag{1.21}$$

where

$$\mathbf{E}_{dip} = k^2 \frac{\mathbf{r} \times (\mathbf{r} \times \mathbf{p})}{\mathbf{r}^3} e^{\mathrm{i}kr} + (1 - \mathrm{i}kr) \frac{\mathbf{r}^2\mathbf{p} - 3\mathbf{r}(\mathbf{r} \cdot \mathbf{p})}{\mathbf{r}^5} e^{\mathrm{i}kr}, \tag{1.22}$$

and the wave vector $k = \dfrac{2\pi}{\lambda}$ [see 37]. We can notice that for the near zone $kr \ll 1$ we acquire the electrostatic result (as in eq. 1.17b). The corresponding magnetic field for the dipole is $\mathbf{H}(t) = \mathbf{H}_{dip} e^{-\mathrm{i}\omega t}$ where

$$\mathbf{H}_{dip} = \frac{ck^2}{4\pi} \frac{\mathbf{r} \times \mathbf{p}}{\mathbf{r}^3} \left(r - \frac{1}{\mathrm{i}k} \right) e^{\mathrm{i}kr}. \tag{1.23}$$

Knowing how the resonantly enhanced polarisation of the sphere effects the EM field, we can look at the accompanying phenomena of enhanced absorption and scattering. Through the knowledge of the Poynting vector

$$\mathbf{S} = \mathbf{E} \times \mathbf{H} \tag{1.24}$$

we can calculate the electromagnetic energy W_a passing through an arbitrary sphere around the particle,

$$W_a = -\int_A \mathbf{S} \cdot \mathbf{e}_r \, \mathrm{d}A. \tag{1.25}$$

The surface of the sphere is A and $\mathbf{e}_r$ is the normal vector of the sphere surface. W_a is the total absorbed energy and can be split for the non absorbing medium in $W_a = W_{ext} - W_s$. We can write the extinction energy as sum of overall (W_a) and scattered (W_s) energy

$$W_{ext} = W_a + W_s. \tag{1.26}$$

From these energies the cross-sections can be calculated [see 25]. The relation 1.26 for the corresponding cross-sections holds in the same manner

$$C_{ext} = C_a + C_s. \tag{1.27}$$

The cross-sections for the quasistatic approximation are then determined as

$$C_s = \frac{k^4}{6\pi} |\alpha|^2 = \frac{9\pi k^4 a^6}{3} \left| \frac{\varepsilon - \varepsilon_m}{\varepsilon + 2\varepsilon_m} \right|^2 \tag{1.28a}$$

$$C_a = k \Im [\alpha] \ = 4\pi k a^3 \Im \left[\frac{\varepsilon - \varepsilon_m}{\varepsilon + 2\varepsilon_m} \right] \tag{1.28b}$$

1.3.2 Mie theory

The Mie theory [first published 38] provides an alternative, more precise and wider approach to solving scattering and absorption by nanoparticles. The theory explains and provides better understanding of the absorption and other optical properties of nanoparticles. This theory is based on scalar and vector functions satisfying the wave equation. The solution using these functions then may be written in the form of Legendre, Bessel, Hankel, and Riccati–Bessel and Riccati–Hankel functions [see 25, 26, 39, 40]. We will not look deep into the calculations and we will present only the resulting coefficients. The theory behind scattering is universally holding the same eq. 1.25, 1.26 and 1.27, only the form of solution is different.

Let's assume a spherical particle of size R and refractive index n_p in an non absorbing medium with refractive index n_m illuminated by the plane wave with wave number $k = \frac{2\pi n_m}{\lambda}$ is placed in electromagnetic field. The scattering coefficients in basis of $\Psi_n(x) = x j_n(x)$ Riccati-Bessel and $\xi_n(x) = x h_n^{(1)}(x)$ Riccati-Hankel functions are

$$a_n = \frac{\Psi_n(x)\Psi_n'(mx) - m\Psi_n'(x)\Psi_n(mx)}{\xi_n(x)\Psi_n'(mx) - m\xi_n'(x)\Psi_n(mx)} \tag{1.29a}$$

$$b_n = \frac{m\Psi_n(x)\Psi_n'(mx) - \Psi_n'(x)\Psi_n(mx)}{m\xi_n(x)\Psi_n'(mx) - \xi_n'(x)\Psi_n(mx)} \tag{1.29b}$$

where m represents the relative refractive index of the nanoparticle $m = \frac{n_p}{n_m}$ and $x = kR$ the size parameter. The refractive index n can be a complex number, which includes absorption in the sphere. The scattering and extinction cross-section are than expressed as

$$C_s = \frac{2\pi}{k^2} \sum_n^{\infty} (2n+1) \left(|a_n|^2 + |b_n|^2 \right) \tag{1.30a}$$

$$C_{ext} = \frac{2\pi}{k^2} \sum_n^{\infty} (2n+1) \Re [a_n + b_n] \,. \tag{1.30b}$$

Using these coefficients we can analytically calculate the spectral characteristics of the nanoparticles.

Chapter 2

Analysis and instrumentation

Preparation and characterization of plasmonic nanostructures requires modern and precise equipment. In order to characterize and evaluate the quality of our nanostructures. The structure parameters were first characterized with dark field microscopy and then with atomic force microscopy. The spectral response of localised plasmons was measured by a spectrometer in transmission geometry and the surface plasmon polaritons were measured in attenuated total reflection setup. The further spectroscopy and sensing utilizing localised plasmon structure was done in a microfluidic chamber.

2.1 Atomic force microscopy

Atomic force microscopy is a method from the family of scanning probe microscopy methods, which is able to image samples surface with nanometre precision. It is widely used in many sectors of physics and biology where such a precision is needed [see 41]. One of its advantages is the possibility of performing the experiment at standard ambient conditions, such as room temperature and atmospheric pressure. Thanks to the ability of measuring samples without any surface treatment, we can also study biological materials in their native function state.

The core principle of the method is based on measuring interaction forces in between the sharp tip and the sample surface. The tip is usually made of silicon with possible coating and it is grown on a thin cantilever. The cantilever is connected to a small plate which serves for mounting the tip to the instrument. The tip is affected by atomic forces and can be either attracted to the sample or repulsed from it. Depending on which of these forces dominates we can distinguish different modes of measurement [see 42]. As an approximation of the force acting between the tip and the sample we can use the Lennard-Jones potential

$$U(r) \sim -\left(\frac{\sigma}{r}\right)^6 + \left(\frac{\sigma}{r}\right)^{12}, \tag{2.1}$$

where σ is a constant setting an equilibrium distance r in between the instrument and the sample. We can distinguish the modes by the working distance,

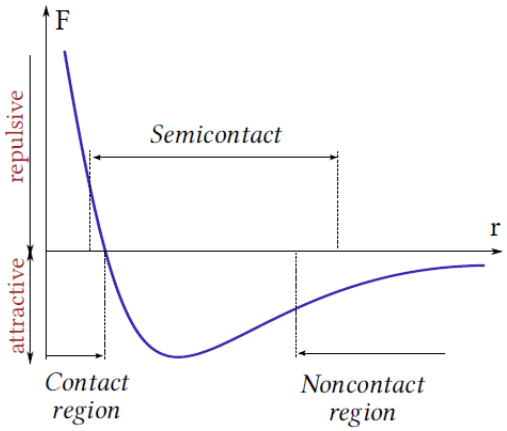

Figure 2.1: Scheme of force acting in between the tip and the sample given by the Lennard-Jones potential. The different modes are distinguished by the distance from the sample [taken from 43].

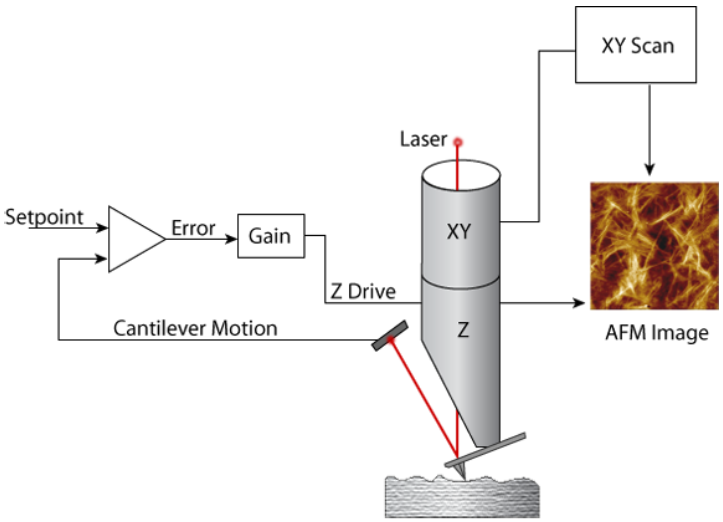

Figure 2.2: Scheme of the atomic force microscope. The feedback loop (left) is correcting the height over the sample and the data are than saved as a topography map (right) [taken from 44].

which is equivalent to the fact, whether the tip is only repulsed/attracted or it experiences both attraction and repulsion (fig. 2.1).

The instrument is measuring the forces acting on the cantilever, and uses feedback loop to correct the distance between the tip and the sample surface as it moves over the sample in xy direction (2.2). The force is derived in each point from the changes in position of laser beam reflected from the cantilever to the photo diode. The setpoint value defines the desired force. The deviation from this value is called error. The error is recalculated using the gain value and sets the z movement response in real time. The information about the z height is saved as the topography map.

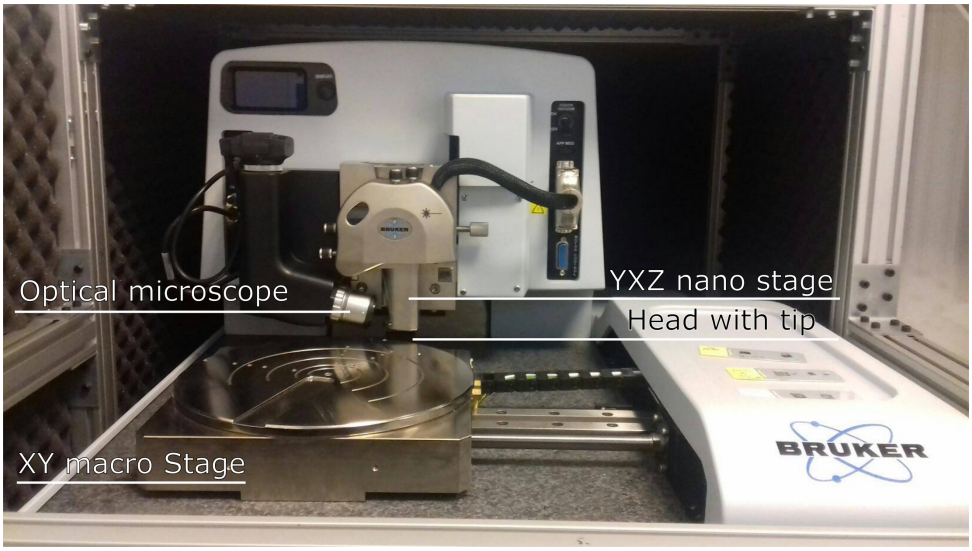

Figure 2.3: AFM instrument used for analysis. The xy movement is governed by two stages, one for loading the sample operating in macroscopic distances and second operating in nanometres, which is built into the head of the microscope together with the z controller. The optical microscope is used for the orientation on the sample and pre-engagement of the tip to the sample surface.

Contact mode. The feedback loop keeps the tip is in constant contact with the sample, therefore there are only repulsive elastic forces acting on the tip. There are two operation options, constant force (feedback loop holds the value of force on a constant value and movement of z drive is proportional to the topography) and a constant height (tip is held at a constant distance from the surface and the force applied on it is proportional to the topography). Constant contact allows us to switch into lithography methods and apply additional force and change the topography. This constant contact may cause higher wear off of the tip.

Semicontact mode. The tip is driven by the alternating current to oscillate on its characteristic frequency. The tip is in contact with the sample only at the bottom of its amplitude. For this characteristics, it is also called the tapping mode. The oscillation is in order of several nanometres, which means the tip is moving from the region of repulsive elastic force to the range where attractive Van der Waals forces take the leading role. The changes of oscillation amplitude are tracked and the z drive compensations correspond to the topography. This mode can achieve higher scanning speeds and it is more sensitive to the biological samples.

In our experiment the tapping mode was used for scans, and the contact mode for performing lithography. The instrument Nanoscope V (Bruker; fig. 2.3) equipped with the software Nanoscope 9 was used together with tips Tap 300 AL-G (Budget sensors) suitable for the tapping mode.

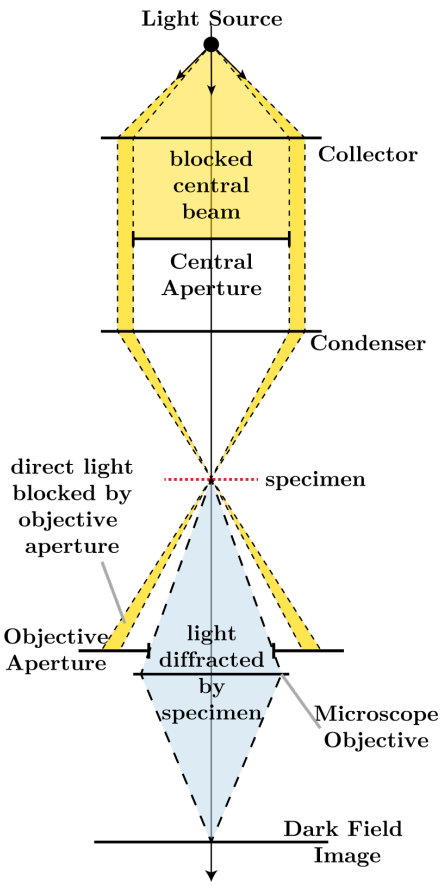

Figure 2.4: Scheme of the dark field microscope [taken from 45]. Light from the high intensity light source is lead to the sample through the collector lenses. First the middle part of the beam is absorbed by the opaque light stop, resulting in a hollow cylinder shaped beam. This beam is then focussed by the condenser lenses on the specimen. The centre of objective collects only the scattered light from the sample and directs it to the ocular or to the CCD camera.

2.2 Dark field microscopy

Another method suitable for imaging the nanoscale structures is dark field microscopy. It is a technique derived from standard optical microscopes with changes in incident angle of the beam. The sample is illuminated under high incident angles and only the light scattered from the sample is collected. This creates the typical appearance of the dark field image, where the structure edges are visible and the background is black.

The scheme of the dark field microscope is shown in fig. 2.4. The scattered light allows us to image particles smaller than the wavelength of incident light. We cannot measure their real size but we can localize single particles, which allows us to make single particle spectra or to analyse the particle distributions.

For our experiment we used the instrument AxioImager Z1m with the

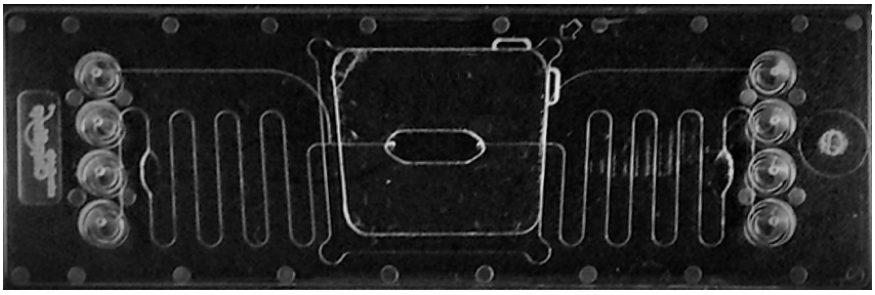

Figure 2.5: The transparent microfluidic chamber on a black background. Chamber with simple two way setup can interchange two fluids. The curved channels (bottom) serve for the incoming fluid and the straight (top) channels ad waste drain.

EC Epiplan objectives and the camera AxioCam MRc5, made by Carl Zeiss microscopy with the software AxioVision from the same producer.

2.3 Spectral measurement

Localized plasmon resonance of the structures was excited by the wide spectral (visible to near infrared) light. There are two possibilities of the spectral measurement: single particle or large surface area. In combination with the dark field microscope we can measure the single particle spectra. The spectrometer is attached to the dark field microscope via an optical fibre and the collected light from the objective is redirected to it. In the experiment we used the spectrometer Acton Research SpectraPro 2300i with the acquisition time of 10 seconds. The grating with 150 grooves/mm centred at 500 nm was used. The transmission arrangement is used with setup for microfluidics or other chamber measurements. Two methods can be used to determine the final absorption I_{abs}. For the first we need to obtain the corrections for the dark current of the spectrometer $I_{dc}(\lambda)$ and the background of the particle I_{bcg}:

$$I_{abs} = 1 - \frac{I_{np} - I_{bcg}}{I_{lamp} - I_{dc}},, \tag{2.2}$$

where the I_{np} is the measured spectra of nanoparticles and I_{lamp} is reference lamp spectra. The second is suitable for the microfluidic measurement and does not require the I_{bcg}. It takes the form of extinction

$$\epsilon(\lambda, t) = \log_{10}\left[\frac{I_{lamp}(\lambda)}{I_{np}(\lambda, t) - I_{dc}(t)}\right], \tag{2.3}$$

where the $I_{np}(\lambda, t)$ is the spectrum acquired in the time t [46]. To overcome possible instabilities of the detector, the background is interpolated linear from the spectral regions beyond the cut-off filters of the spectrometer.

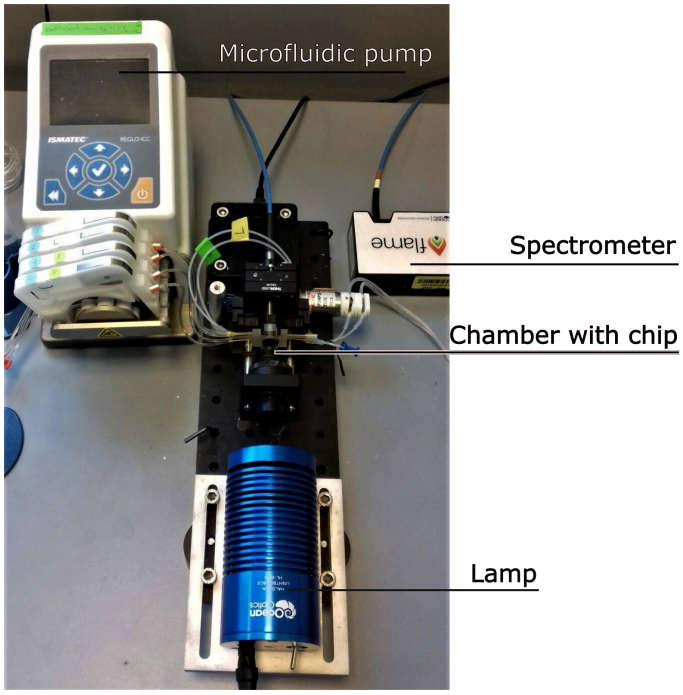

Figure 2.6: The setup for the microfluidic measurement. The optical path goes vertically up from the lamp through the chamber and is collected by the optical fibre leading it into the spectrometer.

2.4 Microfluidics

One of the possible setups for the LSPR sensing is a combination with the microfluidics. This approach utilizes small liquid volumes (lower than μl) which are pumped into a transparent chamber with the LSPR chip. The basic two channel chamber is depicted in fig. 2.5. The two channels provide us control over the medium in the system. First we can observe the bonding of a protein to our structure (change in the local refractive index around our structure) and later apply activation solution and/or buffer with specimen (change in the absorption spectra of the protein). The whole setup can be seen in fig. 2.6.

2.5 Attenuated total reflection

While the localized plasmon polaritons can be excited directly via multispectral light, for the surface plasmon polariton we need to use a coupling method to achieve excitation. The IMI structure of an air/gold/glass prism was used for surface plasmon polariton measurements. The IMI structure is suitable for measurements in the Kretschmann configuration [see 47]. This method utilizes parallel monochromatic laser light with a frequency $\omega < \omega_{sp}$ and scans over the values of projection of the wave vector in x direction k_{px}. The total reflection occurs on the gold/prism interface during scan over the incident

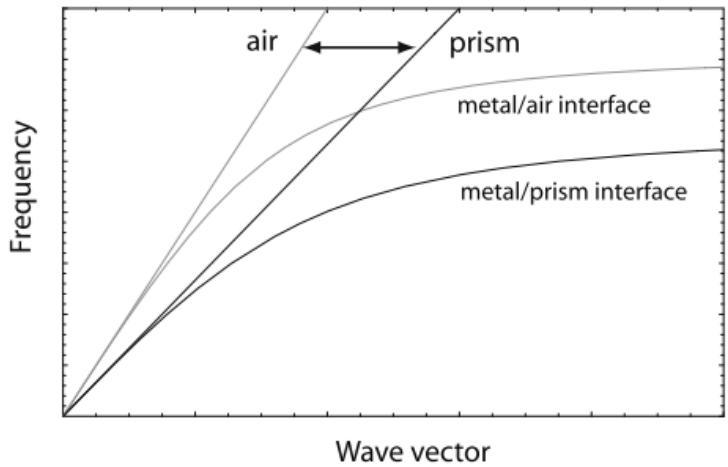

Figure 2.7: The dispersion relations of gold/air, gold/prism interfaces and the light dispersions relation in the two insulator environments. The line marked as prism is referring to the light dispersion relation in the prism. The intersection point of the prism line and the plasmon on gold/air is the coupling condition; therefore it determines the coupling angle of the plasmon polariton.

angle θ. For the coupling of the incident light with plasmon we need to fulfil the coupling condition

$$k_{px} = k\sqrt{\varepsilon_p}\sin\theta, \tag{2.4}$$

where ε_p is the permittivity of the prism. At the coupling angle θ the surface plasmon polariton is excited in the gold/air interface. The coupling is possible thanks to the evanescent wave penetrating through the gold layer allowing it to interact with the plasmon on the gold/air interface (fig. 2.7).

Chapter 3

Experimental methods and design

In order to create a functional LSPR sensor we must consider many parameters, procedures and overall design. At first, we will introduce methods for creating different types of plasmonic structures. Because this work focusses on the possible application in CO sensing we overview the parameters of CO bonding protein myoglobin[1] which can be used as the CO sensitive media. Building on the knowledge of the spectral characteristics of the protein we introduce multiple possibilities for the sensor design. The suitability of the plasmonic nanostructures for sensing purposes is verified by the simulations.

3.1 Methods for structure preparation

There are many ways how to produce plasmonic nanostructures. One of today's very common and used techniques is the electron beam lithography [see 48], but this technique requires a clean room environment and is relatively expensive (regarding time and money). Another less expensive possibility is the nanoimprint lithography [see 49, 50] which still requires a mask created by electron beam. To completely avoid the need use of electron beam we focus on mask methods which use assemblies of nanoscale spheres. Methods using colloid approaches with direct dispension of plasmonic particles were previously tested (reviewed in [51]). The combination with the mask methods should increase the stability of the sensor chips. We will also introduce a method combining the mask approach and atomic force microscope lithography.

All the methods focus on creating chips homogeneously covered with plasmonicaly active golden nanoparticles. The particles can vary in shape, depending on the chosen method, from circular to triangular discs usually in sizes between 70-100 nm and thickness of 20-40 nm.

[1] Myoglobin originating from Equus Caballus (horse). It is a blood protein bonding oxygen as well as carbon oxide.

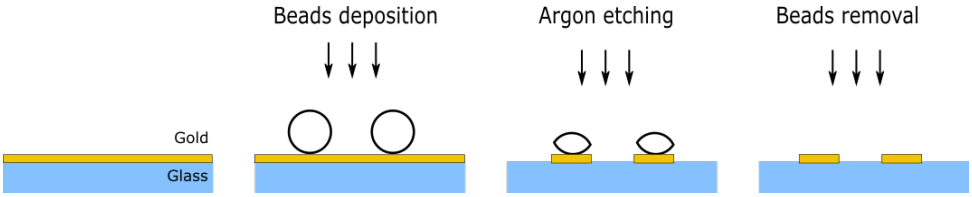

Figure 3.1: Scheme of steps in colloid mask lithography using PS beads. The polystyrene beads are deposited on the glass substrate covered with gold layer. Next the dry argon plasma etching removes the gold layer around the bead mask. And finally the beads are removed, leaving gold discs structure on the substrate.

3.1.1 Colloid mask lithography

One of the simplest methods for creating arrays of circular nanodiscs is the colloid mask lithography. This method uses homogeneously distributed[2] polystyrene or glass nanospheres on a golden layer. Process contains only three steps and is depicted in fig. 3.1. The spheres work as shielding mask for the gold layer during the argon etching and therefore they create the circular shaped disc beneath them. Etching can also be done with non-zero incident angle which causes the resulting shapes of the discs to be elliptical. The way in which the spheres are removed after the etching depends on the type; polystyrene (PS) beads are removed by ultrasonic bath in acetone and glass spheres by tape stripping[3]. The structure is now ready for measurement and sensing.

3.1.2 Inverse colloid mask lithography

The colloid mask lithography can also produce inverse structures, which are in this case circular shaped holes in the golden layer. Theoretically such a inverse structure should have the same plasmonic resonance as the complementary disc structure (Babinet's principle, for example as shown in [52]) while having simple manufacturing process (fig 3.2). The beads are deposited on the clean charged glass substrate and are stripped after deposition of gold, leaving holes underneath them.

3.1.3 Hole-mask litography

Hole-mask lithography is similar to colloid mask lithography but introduces a new additional concept of a sacrificial layer (method first introduced in [22]). This process contains more steps and it has higher laboratory equipment requirements, but it can be modified to provide a broad variety of nanodisc nanostructures.

[2] The process described in section 4.2 on page 33.

[3] Applying an adhesive tape to the surface of the sample captures the beads. The tape is removed and the beads are removed together with it.

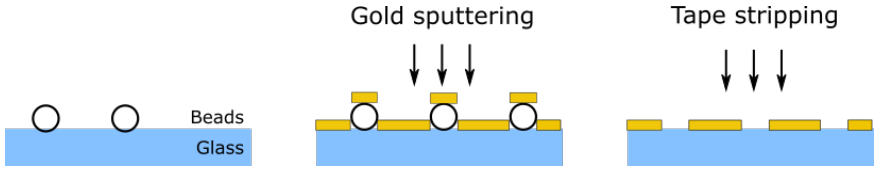

Figure 3.2: Scheme of steps in inverse structure colloid mask lithography using PS beads. The beads are deposited directly on the glass substrate. Subsequently a layer of gold is evaporated over the sample, creating caps over the beads. As the last step the beads with the cap are removed, leaving holes in the gold layer.

The scheme of the procedure steps is shown in fig. 3.3. Nanospheres are homogeneously distributed over the sacrificial polymer layer and gold is evaporated over them. Such a process fills the gaps between spheres and creates cap on each of them. Particles are then removed together with their caps by tape stripping; leaving circular holes in the golden layer (same as creating the inverse structure). The surface is etched by dry etching, which creates holes in the polymer on the areas which are not protected by gold. Another layer of gold is evaporated on top of the remaining layer, as well as in the newly created holes. Finally the sacrificial layer of polymer with the mask is lifted off[4].

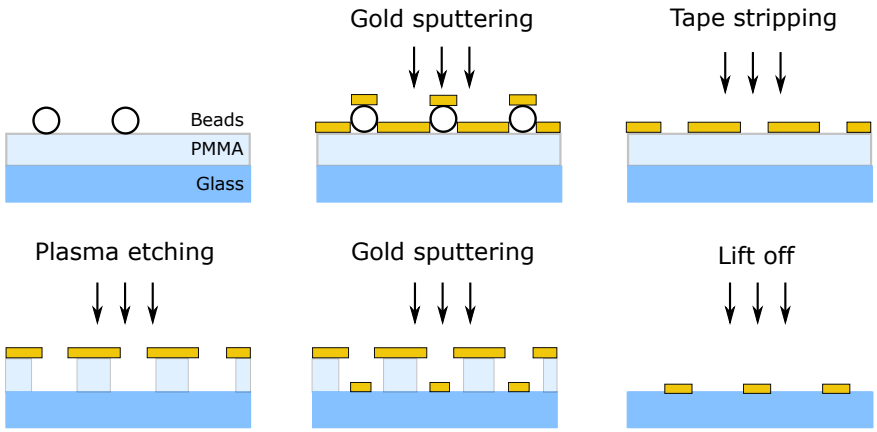

Figure 3.3: Scheme of steps in Hole-mask lithography. The beads are deposited over the sacrificial layer (layer of poly(methyl metakrylate), shortly PMMA). Next a gold layer is evaporated over the sample creating caps over the beads. Further the beads are removed by tape stripping leaving holes serving as a mask for the plasma etching. The holes in the sacrificial layer are created by the etching. Then the deposition of gold creates disc structures on the glass surface. In the end the mask and the sacrificial layer are removed by lift off.

Without any variation the method produces golden discs, another option is tilting the sample during the last deposition step which causes the elliptical shape of the discs. We may also notice that the etching creates holes larger,

[4]The process generally known as lift off is done by dissolving the sacrificial layer in an acetone/isopropanol mixture, removing also the top of the mask.

than are the holes in the gold mask [see 22]. Using several different tilt angles, we can create pairs or triplets of nanodiscs close to each other. Furthermore during long second deposition step the holes in the top layer will gradually shrink, which results in nanocones structure. Combining shrinking hole principle with tilting we can create pairs/triplets of particles with different sizes [see 53].

3.1.4 AFM mask lithography

With the development of atomic force microscope (AFM) techniques we can observe the nanoworld more and more precise. The improvement of the precision is possible thanks to the better piezoelectric positioning units and tips with smaller apex diameter and angle[5]. This development opens more possibilities for precise manufacturing of nanostructures utilizing the AFM analysis and lithography methods. A new lithography method inspired by several of the AFM lithography methods [54–56] combined with hole-mask lithography principle was shortly introduced in my previous work [57] and deserves a closer description.

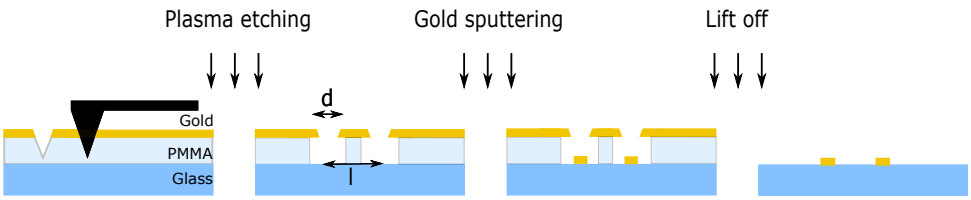

Figure 3.4: Scheme of steps in AFM mask lithography. The PMMA sacrificial layer is coated with gold layer. And the mask pattern is created by the AFM lithography. This opens the possibility to create designed arrays with chosen size d and distances between particles l. Further steps are performed in the same manner as hole-mask lithography; the sacrificial layer is etched, the gold deposited and the mask with the sacrificial layer are lifted off.

The process uses several steps from the hole-mask technique. And the scheme of the process can be seen in fig. 3.4. Substrates are coated with a sacrificial layer and a thin layer of gold is structured by the AFM lithography. Holes of nanoscale size are indented in the gold surface. The created pattern serves as the mask for etching. Dry plasma etching of the sample creates holes in the sacrificial layer. The gold is deposited to create the structure in the same way as for hole-mask lithography. During the lift of in ultrasound bath both the sacrificial layer and the mask are removed. On the glass surface stays only the desired structure.

The mask created by AFM opens possibilities to design patterns and structures with defined coupling. The distances between the particles and the size of the particles is defined by the parameters programmed in the AFM lithography procedure.

[5]These two parameters are stating how 'sharp' is the tip. The sharper is the tip, the lower are the diameter and angle in the apex of the tip.

3.1.5 Microarray spotting

The so far mentioned methods were focusing either on a homogenous film, or on arrays created by AFM. The homogeneous chips are a useful tool in single channel sensing, but to keep up with the measurement requirements of the current biology, chemistry and physics research, we need to have possibility of multichannel sensing. The method of plotting microarrays was shown to be useful as a tool for creating such a multichannel sensing chip directly with the plasmonic nanoparticles from colloid [see 58]. Now we introduce a combination of plotting and mask methods to achieve more stable arrays for consistent analysis.

The creation of microarrays is done by the instrument Nano-Plotter 2.1. The device can dispense sub-nanolitre volumes in a chosen pattern. The small droplets are drying fast and create spots of size around 300 μm in diameter. Such a spot is than viable as one channel of the multichannel sensor.

There are two methods which viable for the spot creation. The first method uses direct dispense of the water solution with PS/silica beads on the golden surface. The water evaporates and the beads stay on the surface. The chip is finished using the same principle as in the colloid mask lithography, but only the spotted areas now have the nanodisc structure. The second possibility is using chips finished by the colloid mask lithography. Such a chip has already a homogeneous distribution over the whole surface. The microarray is created with a polymer glue resist. The resist is UV sensitive and is hardened under UV lamp. The whole chip is etched again removing the homogeneous array not covered by the resist. The resist is then dissolved by acetone-isopropanol mixture, leaving only the gold nanodiscs. The second method achieves higher homogeneity of the spots and prevents the coffee ring effect, but it has an additional step of etching and lift off of the resist.

3.2 Protein overview

The plasmonic structures alone are a good sensing platform. Now we need to utilize their possibility of sensing changes in permittivity. That can be done by using a protein layer, spectrally sensitive on the compound we want to measure. To sense the carbon monoxide we therefore choose myoglobin.

Myoglobin is a protein found in the muscle cells of mammals, already used in multiple different detection methods of carbon monoxide (CO) gas [61]. It has its merit due to its spectral change upon interaction with the CO and relatively good availability. It is a globular protein (fig: 3.5a) with the organometallic compound heme (full name: protoporphyrin IX containing Fe). A simplified scheme of heme is depicted in fig. 3.5b. The molecular weight is 17 kDa and the chain consist of 154 residues. The protein can naturally exist in two oxidation states, which are characterized by the oxidation state of the iron in the heme compound. The Fe^{III} state is the inactive form and the Fe^{II} state is the the active form capable of reacting with oxygen molecules or carbon monoxide (fig. 3.6). The name is changing in dependence

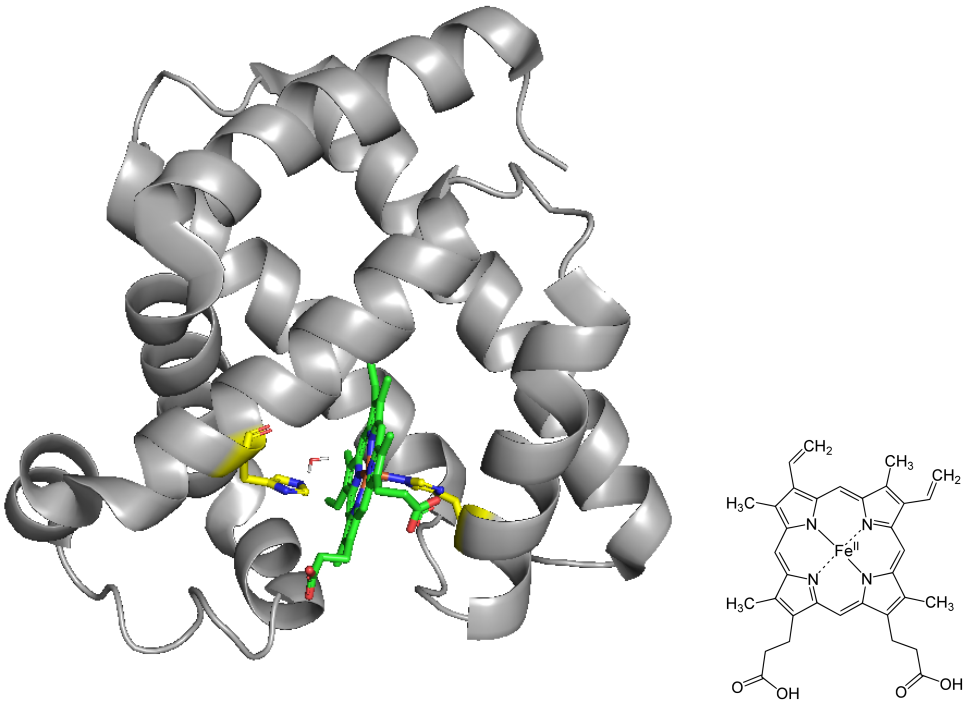

(a) : Myoglobin. **(b) :** Heme.

Figure 3.5: The view of the myoglobin and the organometallic compound of heme. (a): View of the protein structure 5D5R [59] of the deoxymyoglobin with the water in active place. The reaction is moderated by two histidines (yellow); HIS 64 bonding with water (possibly O_2,CO) and HIS 93 bonded to the iron. (b): The simplifies view of the organometallic compound heme.

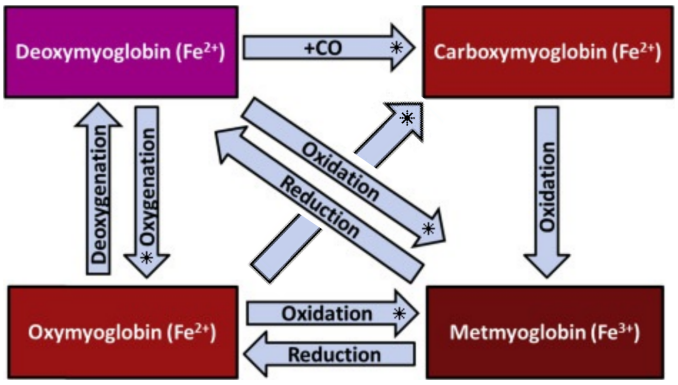

Figure 3.6: Diagram of myoglobin states and most of the possible state transitions. The spontaneous transitions are marked by $*$. The colour of the boxes for the different states represent the colour of the protein. Diagram modified from [60]

of the oxidation state and the bonded compound; metmyoglobin (metMb) for the Fe^{III} state; for the Fe^{II} states: deoxymyoglobin (DMb) without any bond, oxymyoglobin (OMb) bonding with oxygen and carboxymyoglobin (COMb) bonding carbon monoxide. The bond to the heme is moderated

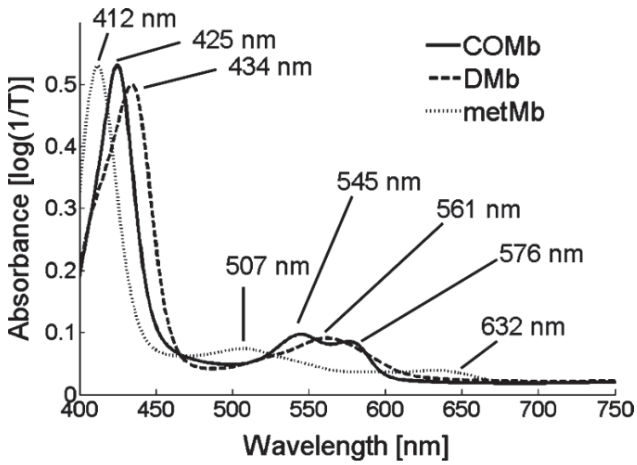

Figure 3.7: The absorbance spectra for three states of the myoglobin protein. The metMb state with the Soret peak at 412 nm and Q-band peaks at 507 nm and 632 nm, the DMb state with Soret peak at 434 nm and one Q-band peak at 561 nm and the COMb state with the Soret peak at 425 nm and Q-band peaks at 545 nm and 576 nm [taken from 66]

by two histidines (HIS), which are directly interacting with the iron or the bonded compound. The HIS 64 and HIS 93 are marked yellow in fig. 3.5a. The active place was also observed in COMb form; the structure from the protein data bank 1DWR [62]. The heme should have slightly different conformation, mainly for the position of the Fe in different states, which was not observable by comparing the two mentioned structures, but other literature refers to it [see 63–65].

3.3 Sensor design

As we have already mentioned, the plasmonic nanostructures are able to sense changes in the permittivity (refraction index as well as absorption index) of the surrounding media. The media is in our case the myoglobin protein, which is spectrally sensitive to its oxidation state. The core principle of the detection is then the spectral change of the protein within the different states. The change in absorption can be characterized by the absorption index κ. It is directly connected to the refractive index n via Kramers-Kronig relations

$$n(\omega) = 1 + \frac{2}{\pi} P \int_0^\infty \frac{\omega' \kappa(\omega')}{\omega'^2 - \omega^2} \, \mathrm{d}\omega' \tag{3.1}$$

$$\kappa(\omega) = -\frac{2\omega}{\pi} P \int_0^\infty \frac{n(\omega') - 1}{\omega'^2 - \omega^2} \, \mathrm{d}\omega', \tag{3.2}$$

where P denotes the principal part of the integral. The relation with permittivity of the media is by definition

$$\varepsilon = n^2 - \kappa^2. \tag{3.3}$$

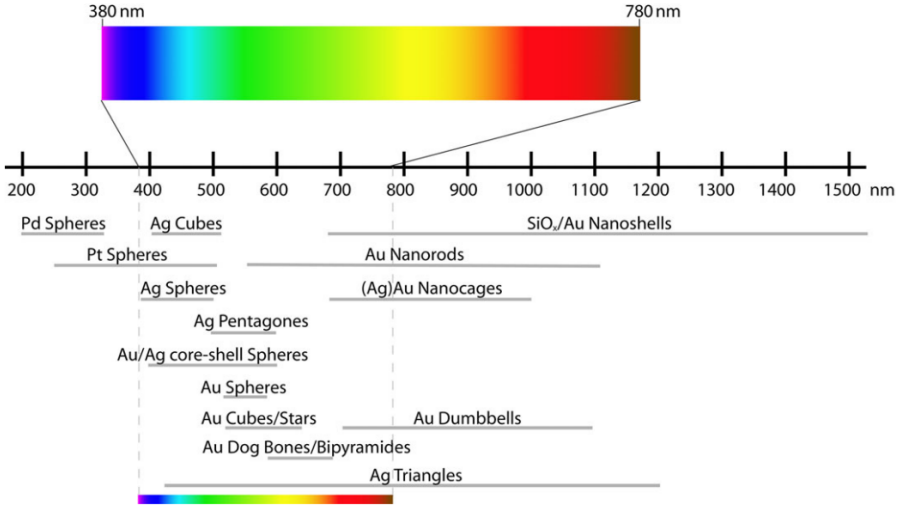

Figure 3.8: The spectral ranges for various types of plasmonic nanostructures. All of the displayed structures were made as colloid solutions. Although the lithography is able to tune the shape and size, none of the pure Au structures is suitable for sensing the Soret peak around 400 nm [taken from 16]

The change in the spectra is most significant in the absorption peak (Soret peak) around 412 nm (for the metMb state), which determines the colour of the protein (fig. 3.7). Although that the Soret peak experiences the largest shift in the spectra, it is not suitable for sensing with plasmonic nanostructures produced by lithography methods. The possible spectral range of the different types of plasmonic nanoparticles can be seen in fig. 3.8. The gold nanodiscs can be tuned to have an plasmonic peak in between 500-800 nm. The detection is therefore aiming at the spectral change of Q-band peaks in the 500-650 nm region.

When we look again at the different states of myoglobin (fig. 3.6) we can notice some of the possible transitions in between of them are spontaneous (marked with $*$). In order to make the most efficient sensor device we want to follow spontaneous paths. The first step is to activate the protein. This process does not occur spontaneously in neutral pH. In order to do so we can reduce the protein (metMb) into DMb by introducing a slightly basic environment such as in blood. In such an environment the DMb then can transition into OMb as well as in COMb state. Additionally, it is important to note that depending on the pH level, a part of the protein can stay in its inactive form or transition back to metMb state via spontaneous paths. In the laboratory environment we have the possibility to use a chemical reaction with sodium dithionite to ensure the full reduction into the DMb state. Sodium dithionite is known for its high redox potential and also reacts with the oxygen in the solution, keeping the protein in the DMb state, allowing it to bond only with CO [see 67, 68]. This allows us to have control over the state of the protein. We can keep the protein with the sodium dithionite to prevent oxygen bonding (stay in DMb state), in order to get

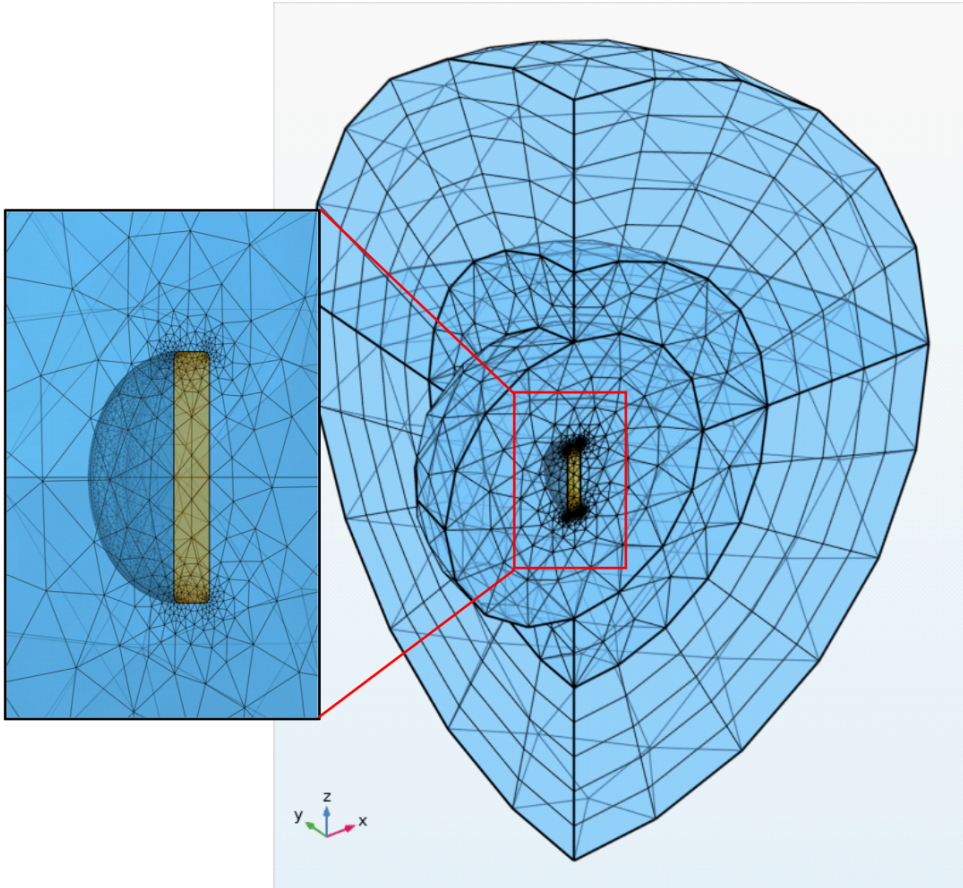

Figure 3.9: Partial view of the nanodisc model with diameter 100 nm and thickness 20 nm. The EM wave propagates in the x direction. The near field extinction was integrated over the surface of the inner sphere.

pure OMb state we need to run the protein through a gel chromatography to separate it from the dithionite salt (assuming that the environment is CO free). In the microfluidic chamber we can remove the dithionite by flushing the chamber with clean buffer solution. Regardless the process, the end state of detection is the COMb state. From the COMb state we can transition back to the inactive metMb form by aplying an oxidation agent, for example a low concentration of ascorbic acid solution or acidic buffer. The DMb and OMb are genuinely time unstable and spontaneously oxidate to the metMb form and become inactive, therefore while making long lasting sensing chip we need to repeat the reduction step or keep the chip in buffer with pH above 7.4 (basic).

3.4 Simulations

The development of a plasmonic nanostructure based sensor is experimentally complex and requires a lot of work and resources. The possibility of using

computer model and simulation provides recently a cheaper and more convenient option for parameter scanning. With use of theory we can create a model of sphere or nanodisc structures of any shape, size and material. The simulation for our experiment were done in the COMSOL multiphysics program. With the module for wave optics we calculated extinction cross-section of the nanodisc model with diameters 100 and 70 nm and heights 20 and 40 nm. The program utilizes finite element method in order to solve the differential equations for EM wave with the boundary conditions of the system. The particle model (fig. 3.9) consists of multiple layers. The inner disc is gold material from the COMSOL library. And the outer media is defined by the constant refractive index followed by multiple perfectly matched layers (PML) of the same properties. The disc can be optionally surrounded by a thin layer of absorbing media simulating the protein layer. The layer of 5 nm (thickness estimated from the protein dimension) was modelled with the permittivity calculated via Krammers-Kronig relations and measured absorbance data. To avoid the sharp edge effects the edges of the disc were smoothed with the radius of 5 mm. The meshing is tetrahedral with higher density to the edges of the disc to have more precise data at the points of interest.

Chapter 4

Results and discussion

The proposed methods require a lot of experimental optimization and careful analysis. Many experiments were carried out and the example data with the analysis procedures are shown. The discussion is then provided taking in consideration all the results. The discussion is made for each of the important procedure steps and for each of the methods separately. Changes and improvements for further research are proposed.

4.1 Simulations

We have already mentioned that the simulations can be a powerful tool to save time and resources during the experiment. To ensure that the numerical results are corresponding with the theory, an example simulation of plasmonic particle was calculated. An extinction cross-section of 100 nm golden sphere can be calculated by the finite element method in COMSOL via general equations describing a scattering particle (eq. 1.25, 1.27 on page 12) as well as directly from the analytical formula given by Mie theory (eq. 1.30b on page 13) evaluated by Matlab. The model was calculated for two different indices of refraction of the surrounding media and the resulting extinction cross-sections (fig. 4.1) are showing difference smaller than 1%. The small difference is mostly due to intensity changes out of the resonance peak area.

The analytical results are only available for basic geometries; therefore the further extinction cross-section of the disc models can be only calculated via the direct solving of equations by the finite element method. The results of those simulations will be shown in the sections with the corresponding experimental results.

4.2 Homogeneous assembly

4.2.1 Principle

For the methods utilizing the colloid as the mask, it was necessary to create a homogeneous assembly of polystyrene/silica beads on the sample surface. The homogeneity of the random assembly ensures that the particle interaction

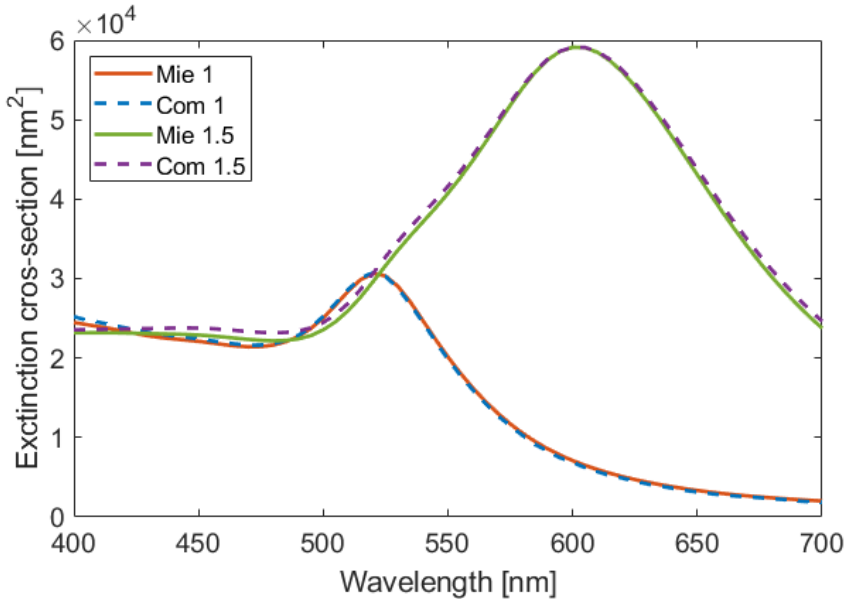

Figure 4.1: Extinction cross section of a 100 nm gold sphere calculated by COMSOL and evaluated by Matlab from Mie theory. The solid lines show the theoretical results for two different indices of refraction of the surrounding media; 1 for air and 1.5 for glass. The dashed lines show results from the finite element calculations in COMSOL for the respective environments.

is reduced and there is no constructive crosstalk caused by arrays interaction or coupling. The substrates were prepared with a positively surface charge mediated by the PDDA polyelectrolyte[1]. The beads are dispersed in a solution and are surface functionalised by the COOH group, which dissociates in water into COO^- (and H^+). The particles are repelling each other and simultaneously they are spontaneously attracted to the positively charged surface of the substrate. This way we can ensure homogeneous distribution with high stability during further procedures.

To optimize the process, the following parameters were varied: ozone plasma treatment time, concentration of PDDA polyelectrolyte, weight concentration of 100 nm PS nanoparticles in water (span from 0.5 wt% to 0.0005 wt%) and time of deposition of nanoparticles (1, 2 and 5 minutes). During polystyrene beads deposition, samples were always completely covered by solution droplet of volume 200 μl.

4.2.2 Analysis

The homogeneity of the resulting layer was first examined by the dark field imaging for higher concentrations of PS spheres (fig. 4.2). From observations made during the experiments, the importance of proper removal of beads not attached to the surface by rinsing is obvious, due to prevention of the coffee ring effect [69]. The rinsing has been therefore applied to each of the further

[1]Detailed description of the procedures are described in section A.1on page 65

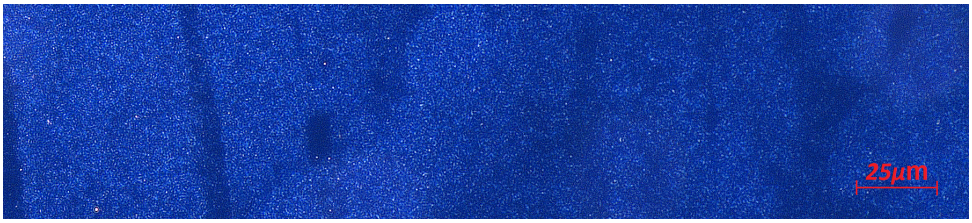

(a) : Washed

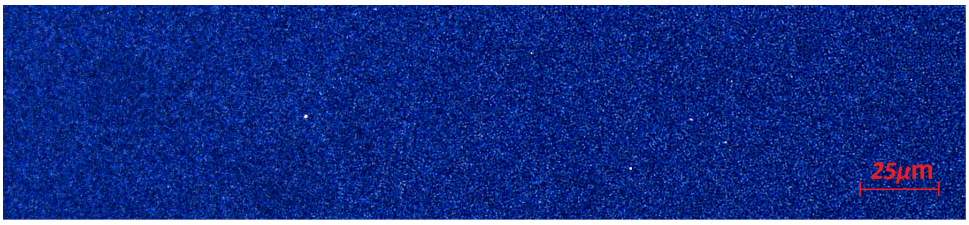

(b) : Washed and rinsed

Figure 4.2: Effect of water rinsing on the sample covered with layer of 100 nm PS beads deposited from 0.5 wt% water solution. Before the deposition, the substrate was pre-treated for 5 minutes in ozone cleaner and then exposed to 0.2 wt% solution of PDDA.

on prepared samples, in order to ensure its optical homogeneity.

At closer inspection by AFM we could study the homogeneity on smaller scale. This type of measurement would not be representative for the whole sample if the sample would not be homogeneous at larger scales. The homogeneity on smaller scale was determined by the nearest neighbour distance (distance from centre to centre of closest particle). The final quality of the structure is quantified by an aggregation of particles (%) and the density of particles (bead/μm^2). Both of these parameters were extracted from the topography of the samples with deposited beads. Topography scans were processed in open source program Gwydion [published in 70]. Data were levelled with subtracting a tilted plane in order to have zero height of background. Particles were localized by overlapping of two filters. Watershed method was used in order to distinguish particles close to each other (fig. 4.3a). Threshold method was applied with two parameters; diameter of the particle (to eliminate the particles smaller than 5 nm in diameter caused by errors in AFM measurement) and height (to eliminate the phantom particles found by the watershed on the background level); step shown in fig. 4.3b. Coordinates of the centres of particles were exported (4.3c) and processed in Matlab into histograms stating the nearest neighbour distance (fig. 4.3d). The nearest neighbour distance is than used to calculate the aggregation of particles. The particle is marked as aggregated if the surface of another particle is closer than 25 nm. This distance is in the nearest neighbour graphs 125 nm as it shows the measurement between the centres of the particles. The condition is visualized by crosses in fig. 4.3c. The density of particles is simply derived from the total amount of particles divided by the area.

In order to optimize the final aggregation and density parameters, a series

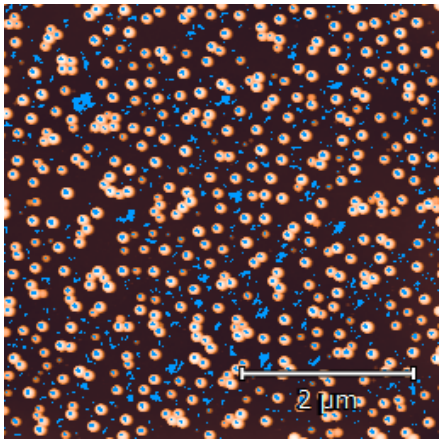

(a) : AFM image with the mask (blue) created by the watershed method.

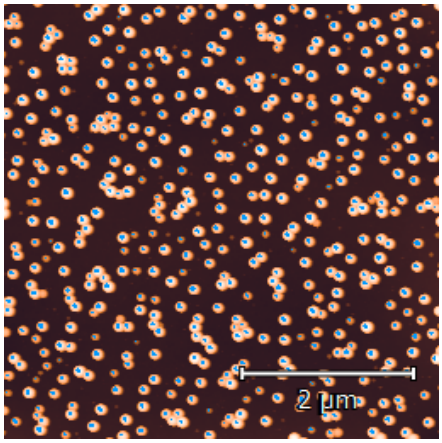

(b) : AFM image with the mask (blue) after applying the threshold level.

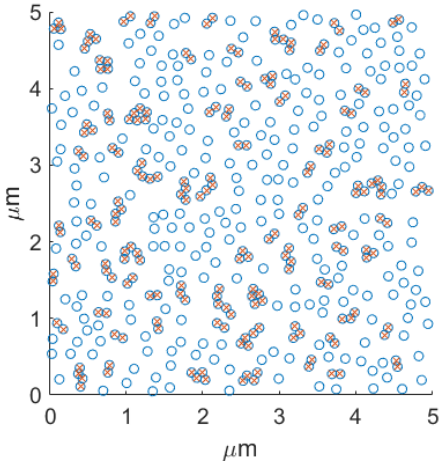

(c) : The plot based on central coordinates exported from the Gwydion analysis. The particles marked by cross have nearest neighbour within the 125 nm distance and are considered as aggregated.

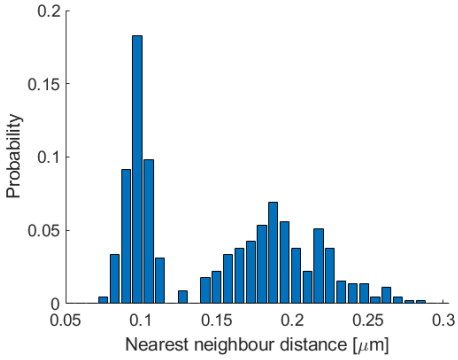

(d) : Nearest neighbour distance based on central coordinates exported from the Gwydion analysis. The first peak around 0.1 μm corresponds to aggregated particles.

Figure 4.3: Sample with 100 nm PS beads in concentration of 0.05 wt% for 2 minutes, previously treated 5 min in ozone cleaner with 0.2 wt% of PDDA. Aggregation is 44% and the density 18 bead/μm^2.

of samples was prepared differing in the deposition time and the PS beads concentration. Starting at higher concentrations (fig. 4.4) we can observe high aggregation (the sample corresponds to the one shown on the dark field image in fig. 4.2b), so we are sure that optical homogeneity is not necessarily transported to smaller scale. The majority of the particles are aggregated presumably due to the high concentration of the solution. With decreasing concentration (other parameters fixed), we can observe less aggregation (fig. 4.3d; the example case for the analysis). A similar effect is observed also with the variation of the PS beads deposition time (data shown only in the summary table 4.1).

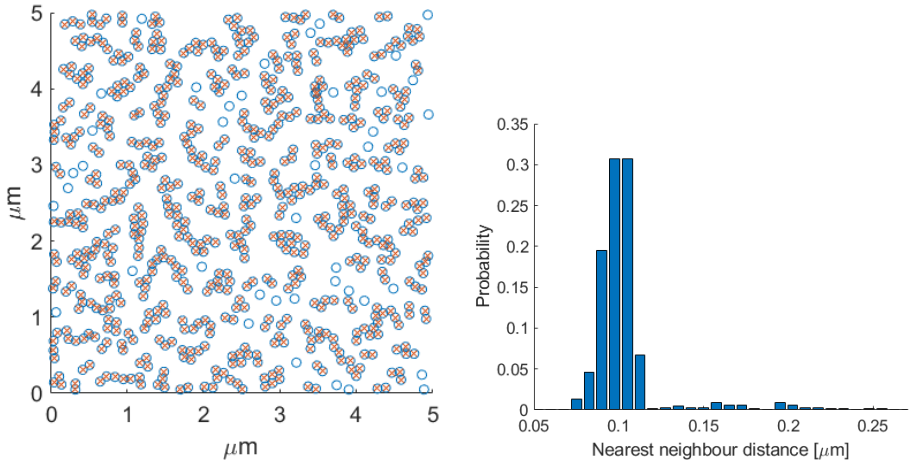

(a) : The plot based on central coordinates exported from the Gwydion analysis. The particles marked by cross have nearest neighbour within the 125 nm and are considered aggregated.

(b) : Nearest neighbour distance based on central coordinates exported from the Gwydion analysis. The first peak around 0.1 μm corresponds to aggregated particles.

Figure 4.4: Sample with 100 nm PS beads in concentration of 0.5 wt% with 1 minute deposition time, previously treated 5 min in ozone cleaner with 0.2 wt% of PDDA. Aggregation is 94% and the density 28 bead/μm^2.

Table 4.1: Comparison of aggregation and density for different sample parameters. In the results from 1 minute deposition time, we can see the effect of increasing density of PS beads. The results for concentration 0.0005% then offer comparison for the different deposition times. The * shows result of the same processes on the PMMA layer. The step of shaking during the deposition was added, resulting into denser, less aggregated assembly.

Deposition [wt%]	0.5	0.05	0.005	0.0005	0.0005	0.0005	0.05	0.005
time [min]	1	1	1	1	2	5	2*	2*
Aggregation [%]	94	44	14	2.5	2.8	7	35	1
Density [bead/μm^2]	28	18	7	2	2.6	3.3	21	6

The optimization of the aggregation is easily achieved by lowering the concentration of the PS beads solution, but by lowering this parameter the density decreases as well. Low density is not preferable for the final structure, as it is directly connected to the strength of the plasmonic response. For the final structures, we must therefore balance the parasitic plasmonic response caused by aggregation and the total strength of response provided by the sufficient density of the desired plasmonic structures.

The same processes were then tested on substrates for the hole-mask lithography. The material on which we deposit the beads is now poly(methyl metacrylate) − PMMA coated glass (fig. 4.5). In order to acquire comparable results, we needed to increase the ozone cleaner treatment time to 10 minutes. The lower efectivity of the ozone cleaner may be caused by the different

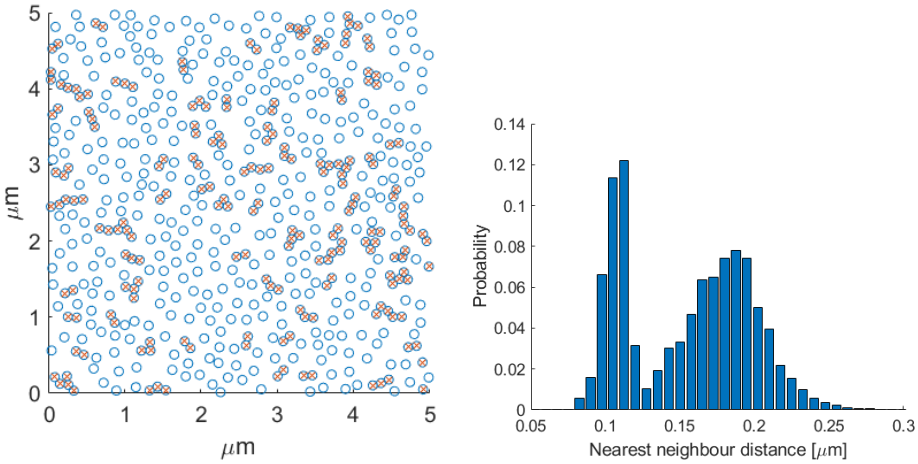

(a) : The plot based on central coordinates exported from the Gwydion analysis. The particles marked by cross have nearest neighbour within the 125 nm and are considered aggregated.

(b) : Nearest neighbour distance based on central coordinates exported from the Gwydion analysis. The first peak around 0.1 μm corresponds to aggregated particles.

Figure 4.5: Sample with 100 nm PS beads in concentration of 0.05 wt% with 1 minute deposition time on PMMA layer, previously treated 10 min in ozone cleaner with 0.2 wt% of PDDA. The sample was shaked during the PS beads deposition. Aggregation is 35% and the density 21 bead/μm^2.

surface behaviour of the polymer in comparison to glass, where the procedure gives reliable results. A new procedural step of shaking during the PS beads deposition was tested, resulting in higher density of the structure with lower percentage of aggregation.

In further depositions, the following parameters were used: 0.2 wt% of the PDDA solution, deposition of PS bead solution with 0.05 wt% concentration for two minutes and shaking during the deposition. The sonication of the beads was additionally introduced for possible reduction of the aggregation of the beads before deposition. The chip was rinsed with flowing distilled water[2].

4.3 Gold deposition and thin film measurement

The mask process for manufacturing plasmonic nanostructures and thin films always contains the step of gold deposition. In the experiment we used PVD method of vapour deposition. The working vacuum was provided by a combination of a rotary pump and a diffusion pump (10^{-3}Pa) or by a turbomolecular pump (10^{-5} Pa) depending on the available equipment. The gold was vaporized by ohmic heating in a small filament boat connected

[2]This is the first time in the process where once distilled water is used. The previous steps were dealing with surface charges, so the use of Mili-Q water is necessary to prevent neutralization.

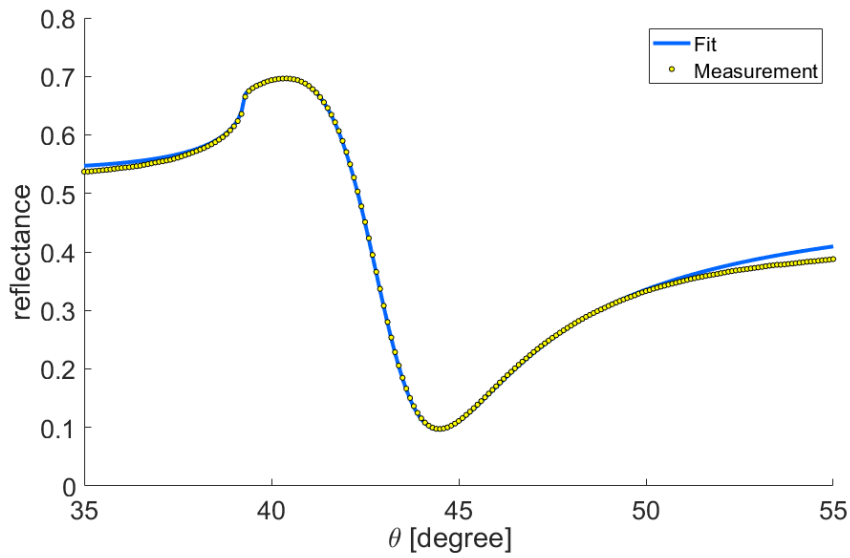

Figure 4.6: Attenuated total reflection of the calibration gold layer. Data measured with 2θ goniometer setup and He-Ne laser of λ= 632.8 nm in p polarisation.

to the electrodes with high current. As an adhesive layer under the plasmonic gold layer, the layer of chromium or titan in thickness around 4 nm was evaporated. Chromium and titan interfere slightly with the plasmonic properties but the benefit of enhancing adhesion of the gold overweights the drawbacks[3].

The PVD system needed to be calibrated in order to ensure the deposition of a layer of desired thickness. The control over the amount of deposited material is ensured by crystal resonator, which changes natural resonation frequency linear with the weight change during the deposition. By depositing and measuring the thickness of a calibration layer, we can determine the calibration coefficient c_e in between the thickness d and the change of oscillation frequency of the crystal Δf.

$$d = c_e \cdot \Delta f \tag{4.1}$$

The calibration layer was tested by two methods. The first method utilizes the plasmonic properties of a gold layer. Attenuated total reflection method (ATR) is used for measuring angle θ reflectivity dependence of a gold layer in a 2θ arrangement. The layer parameters thickness d and permittivity ε', ε'' are then fitted according to the theory utilizing Fresnel equations [see 71].

The measurement can be seen in fig. 4.6 and the corresponding fitted parameters are in table 4.2. We can notice that the resulting value of ε' and ε'' are different from the bulk values from literature. The fitted values difference is showing the quality of the golden layer. The smaller value of ε' is

[3]The higher stability achieved by the adhesion is mostly visible in possibility to reuse and clean the samples for measurement. The plasmonic chips were cleaned in ultrasound bath repetitively to perform different protein measurements.

Table 4.2: Parameters resulting from ATR data fit and literature data for 632.8 nm of bulk gold [taken from 30].

Fit	Value	Literature	Value
ε'	-9.1	ε'_l	-11.685
ε''	3.1	ε''_l	1.267
d	488 Å		

genuinely making the plasmonic exchange less effective as it influences the dispersion relation [see 72]. The dispersion relation depends also on the thickness of the layer [see 73]. The difference in the bulk and layer is not a mistake in the measurement/fit, but it naturally arises from the quality of the layer, which is mainly given by the purity of the material. The working vacuum of 10^{-3} Pa is on the edge of high vacuum level, this can result in unknown impurities occurring in the gold layer and possible contamination by the adhesive material.

To sum up the result of the calibration - the sample was evaporated with frequency change $\Delta f = 2.96$ Hz. The fit has determined the thickness of 27 nm, leading to a calibration coefficient $c_{e1} = 16.48$ nm·s which is stating the thickness deposited per 1 Hz change of the crystal resonator frequency.

For comparison, the second method used a non-optical method of SAX reflectivity. The sample is irradiated by Cu K-alpha X-rays (1.54Å) and the reflectivity under a small angle in 2θ setup was measured (fig. 4.7). The data were fitted by the GenX program [74], where the important parameters fitted were the thickness $d_{Au,Cr}$ of both Au and Cr layers and the roughness σ of the interface (table 4.3). The most important parameter for the thickness of the layer are the angular differences $\Delta\theta$ between the neighbouring maxima [theory from 75].

The SAX method does not look at all at the optical properties of the material. The impurities in the film are represented by the roughness σ and the density of the material. The density fit was calculated as well, but the value did not differ from the table value within the stability of the fit. The resulting calibration coefficient $c_{e2} = 14.36$ nm·s differs 13 % from the $c_{e1} = 16.48$ determined by the ATR data fit. The difference is not significant and is caused by different fitting according to different theories.

In the deposition for further plasmonic nanostructure we have chosen $\Delta f = 1.5$ to achieve the thickness of the gold slightly over the 20 nm. According to $c_{e1,2}$, the structure should have 24.72 nm from the plasmonic fit and 21.5 nm from the SAX fit.

From the AFM analysis (fig. 4.8, 4.9) of one of the resulting structures with deposition parameter $\Delta f = 1,524$, we can say that the resulting depth was 24 nm with 1.2 nm roughness. If we count that the AFM imaging is providing the most relevant results, the calibration expected value was 4.6 % higher for ATR and 8.3 % lower for SAX calibration.

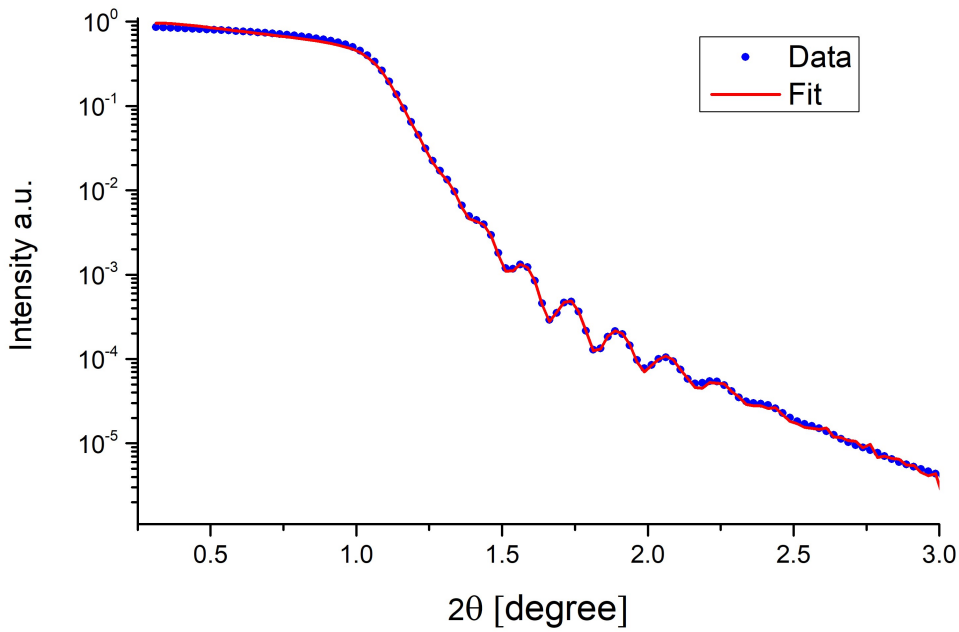

Figure 4.7: The fitted data from SAX measurement in 2θ arrangement from the same sample as used for ATR.

Table 4.3: Parameters resulting from XRD data fit.

Fit	Value
d_{Au}	425 Å
d_{Cr}	21 Å
σ	12 Å

4.4 Inverse colloid mask lithography

After the calibration gold deposition we can use the optimized parameters for the homogeneous assembly to produce the inverse disc structure. The glass substrate was adequately cleaned and charged negatively by a bath in diluted chromic acid cleansing mixture[4]. The positive charging is then mediated by PDDA polyelectrolyte. The 100 nm polystyrene COO^- charged beads were used.

Resulting structure was analysed by the AFM microscopy (fig. 4.8a, 4.8b) and the transmission absorption spectra was measured (fig 4.10). The layer was evaporated based on the calibration process and the thickness of the layer determined from the cut of the AFM image (fig. 4.9). The obtained value was determined to be 24 nm with the root mean square roughness of 1.2 nm (determined by the Gwydion analysis). The mean square of roughness

[4]The process is used instead of previously described process with ozone cleaner A.1 due to the inaccessibility of the equipment.

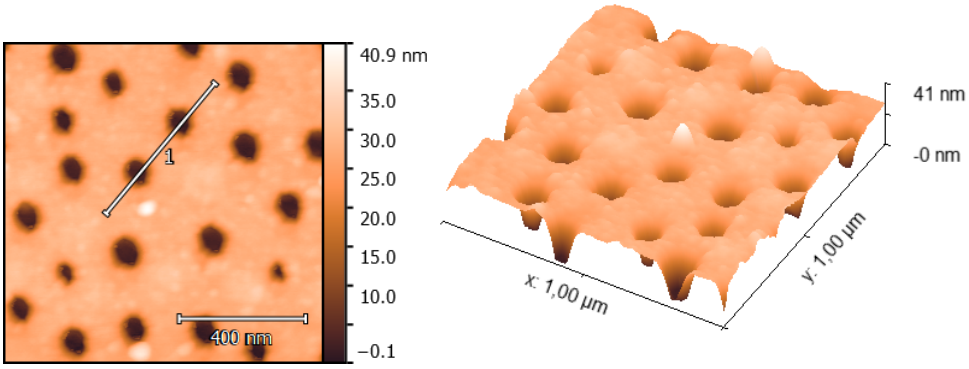

(a) : AFM image of the structure produced by inverse colloid mask lithography. The line 1 is cut through the data and it is shown in graph 4.9. We can also notice the slight roughness of the surface visible as lighter spots within the height around 30 nm.

(b) : 3D projection of the same AFM image (a) turned by 120° to give an insight into a structure of the edge holes. The roughness (1.2 nm) is also noticeable. Note that the x,y and z axis are far from equal. The reducing diameter of the holes from the surface is caused by the convolution with the tip.

Figure 4.8: The AFM analysis data from inverse colloid mask structure.

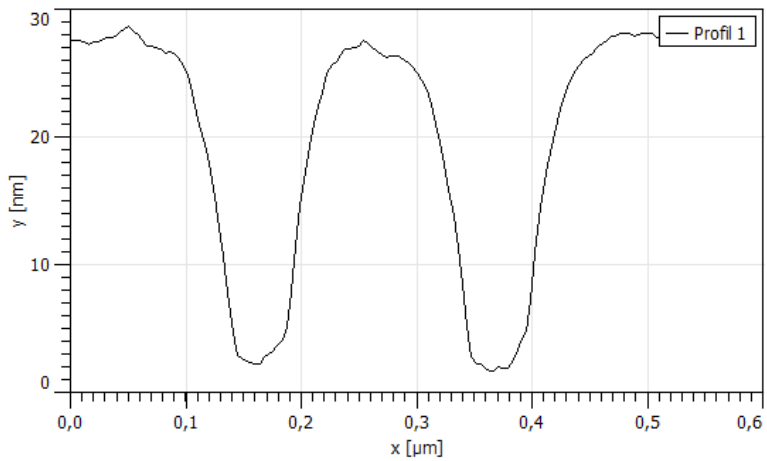

Figure 4.9: The example profile of the cut along the line 1 in fig. 4.8a. From the data we determined the thickness of the layer to be 24 nm with the mean square of roughness 1.2 nm. The diameter of the hole can be determined from the height around $y = 20$ where the convolution of the tip with the sample is negligible and the obtained value is slightly under 100 nm.

is corresponding to the GenX fit of roughness (12 Å) of the previous layers deposited by the same machine. The expected thickness calculated from calibration was 4.6 % higher for ATR and 8.3 % lower for SAX calibration. We can also see that the diameter of the holes is not homogeneous, the average diameter of the hole is 100 nm and standard deviation 20 nm (not considering aggregations). The change in diameter can be caused by the uneven deposition of the gold.

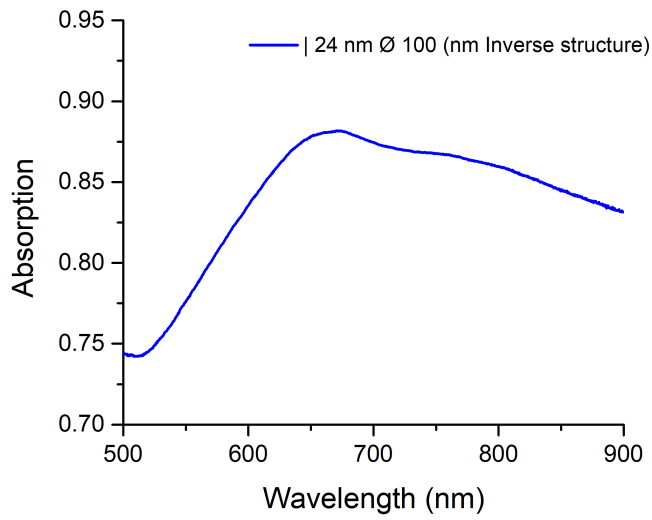

Figure 4.10: Absorption spectra of the hole structure measured in transmission mode in reference to air. We can observe wide peak caused by the inhomogeneity of the hole diameter with high background (0.7) corresponding to absorption of the 24 nm golden layer itself.

The inhomogeneity of the hole diameter strongly influences the quality of the spectra (fig 4.10). The absorption spectra is very broad due to the high amount of structures with different positions of the absorption maxima. We can notice the main peak around 680 nm which corresponds to the disc structures of the same diameter (fig 4.21 on page 50). The very broad spectrum and high background absorption is problematic for the use in the plasmonic sensor. We need to be able to locate and track the absorption maxima precisely, which becomes harder with broad spectra.

4.5 Hole-mask lithography

For the hole-mask lithography we used substrates with the PMMA layer[5]. The homogeneous assembly of 100 nm PS beads was created with the optimized procedure parameters; taking in consideration the prolonged oxygen treatment time of the PMMA layer. As the covering mask over the beads, the adhesive Ti layer and Ag layer was evaporated in total thickness of 30 nm. The tape stripping of the beads from the surface was performed and the inspection of the stripped chips was done by both SEM and AFM. In fig. 4.11, we can see the differences between areas unaffected by the tape stripping and stripped areas. The effectiveness of the tape stripping was less than 100%. To ensure that most of the sample is stripped, the process was repeated multiple times for each chip. We must be cautious not to strip the whole metal layer while it is exposed to the repetitive stress by tape stripping. The tape

[5]The preparation process is described in detail in section A.1on page 65.

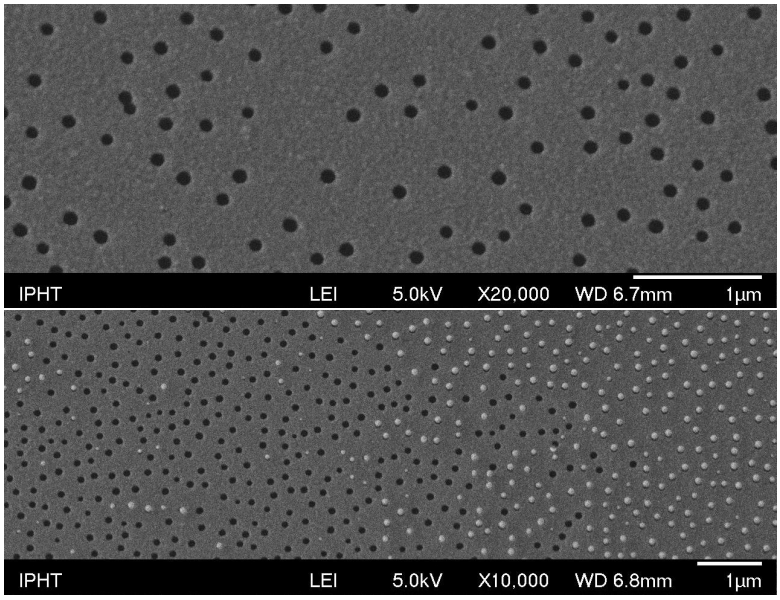

Figure 4.11: SEM images of tape stripped sample. The completely removed area (top) and partially stripped area (bottom).

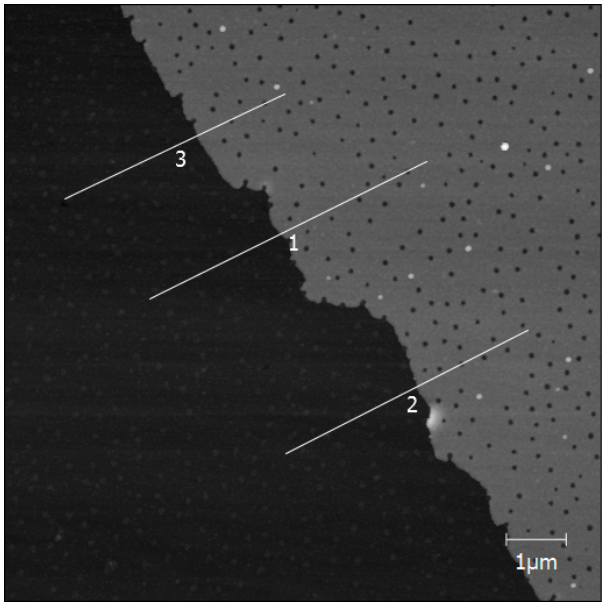

Figure 4.12: AFM scan of tape stripped sample with the area of completely removed metallic layer. The hole structure is visible on the right side of the sample scan.

stripping should be done continuously and slowly to prevent the layer damage; stripping of the mask layer (fig. 4.12). We can also notice inhomogeneity in the size of the particles. The inhomogeneity is noticeably lower than for the inverse colloid mask method. The layer was evaporated on different instruments and particles from the same company were used. Therefore,

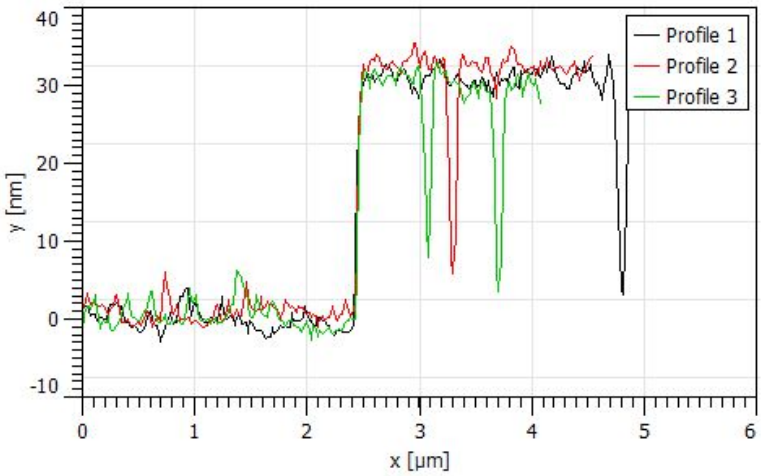

Figure 4.13: Profiles cuts along the lines 1, 2 and 3 in fig. 4.12.

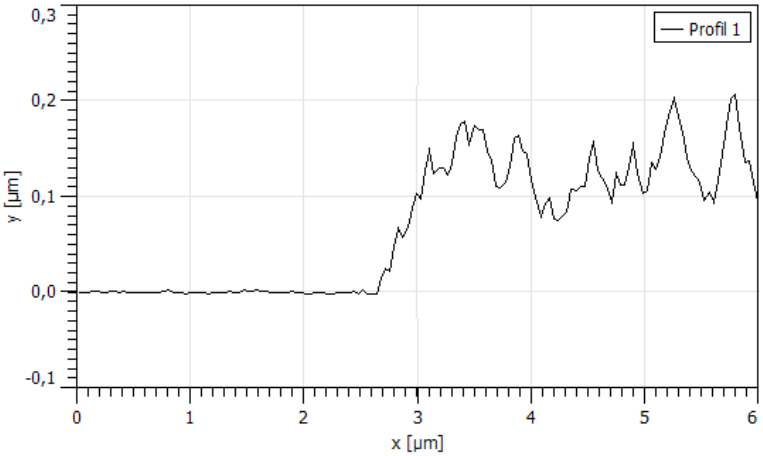

Figure 4.14: The profile of the interface from fig. 4.12 after O-RIE. The thickness of 170 nm of PMMA was etched. The mask surface shows high disruptions caused by etching.

we can say that the higher inhomogeneity was mostly caused by the used instrument.

When we look at the cuts from the stripped areas, we can measure the real thickness of deposited metals and the holes left after PS beads (fig. 4.13). The topography measurement gives the total deposited layer thickness of 30 nm. We can see that the depth of the holes is not measured precisely due to the convolution of the tip with the topography.

Hole mask is then prepared by oxygen reactive ion etching (O-RIE) for one minute at the power 128 W. After etching, the AFM inspection was made, and the key problem of the process appeared. On the areas where the PMMA layer was not covered by the mask, the etching was homogeneous up to the glass surface as expected. Within the silver mask, oxygen plasma caused severe disruption in the mask surface and growth of silver oxide.

Fig. 4.14 shows an AFM measurment of the uneven surface of the mask. Roughnes of the surface is around 100 nm.

With such destroyed mask the process could not continue. We propose further change of the protocol by exchanging the silver mask layer for some more resistant metal or change the method of etching.

4.6 AFM mask lithography

AFM mask lithography utilizes the sacrificial layer principle together with AFM lithography. Special substrates were made to test the new technique. The sacrificial layer of PMMA on a glass wafer was covered by 3 nm of titan and 20 nm of gold. The substrate wafer needed to be covered with a varnish in order to be cut in smaller chips[6]. The varnish needed to be removed properly from the chips in order to ensure a reproducible lithography process. During the varnish removal process in the ultrasound bath, the gold layer detached due to its insufficient adhesion to the PMMA layer. More gentle method with only submerging the substrates into the solvent have not prevented the layer detachment. To avoid the varnish removal process before performing the AFM lithography, new method for creating substrates was necessary. The substrates for hole-mask lithography were cleaned and the golden layer with titanium as adhesion layer was evaporated over it. With the surface prepared in such way, the lithography could be executed. Patterns were indented into the layer by AFM probes with 10 nm radius at the tip. The AFM lithography mode works with the parameter of z-shift corresponding to movement of the tip closer to the sample than the distance for the contact mode. A set of holes with increasing z-shift was indented. Three arrays with increasing z shift were produced using the same tip (fig. 4.15).

We could estimate approximate depth of holes from the AFM picture made by the same tip (fig.4.16) It is obvious that the measured depth is not the real one, because of convolution in between the sample surface and the tip. The dependence is linear in the tested range, so we can conclude that the material is soft enough and does not bend the cantilever. We can use the upper estimate limit and conclude that the approximately 150 nm z-shift can penetrate the 20 nm golden layer. Another estimate of the depth of the hole can be made from the shape of the tip set by the producer. The tip should have 10 degrees cone angle at the apex. From the hole size of 100 nm for 100 nm z-shift, we can conclude that also smaller z-shift values should penetrate the golden layer.

Knowing the approximate z shift in which the indentation could be done, the protocol for the AFM instrument Nanoscope 9 with the lithography mode Nanoman was prepared. The AFM device was set into highest resolution of 3200 lines on 80μm scan size, resulting in the step size of 25 nm. A mesh of holes with different spacing was created in Matlab and the annotations were added (fig. 4.17).

[6]The process is described in detail in section A.1on page 65.

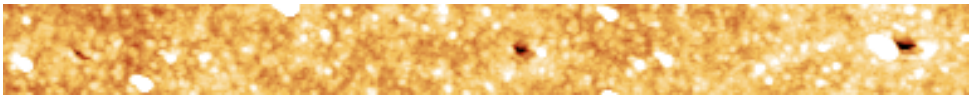

(a) : From left: 50 nm z-shift (x $\sim 0,25\mu m$), 75 nm z-shift (x $\sim 1.51\mu m$), 100 nm z-shift (x $\sim 2.8\mu m$)

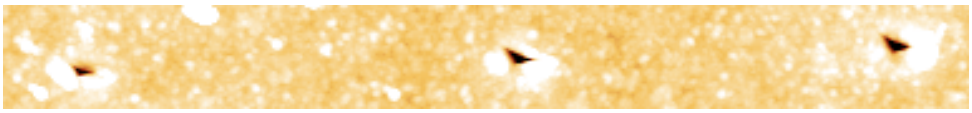

(b) : From left: 125 nm z-shift, 150 nm z-shift, 175 nm z-shift

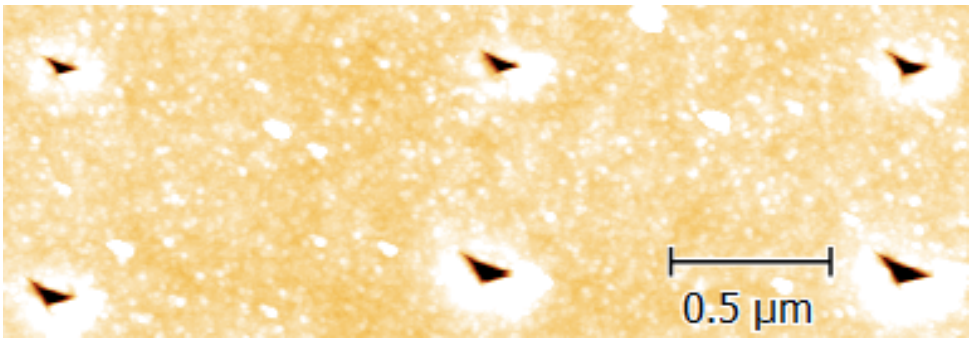

(c) : First row: 200 nm z-shift, 225 nm z-shift, 250 nm z-shift. Second row: 275 nm z-shift, 300 nm z-shift, 325 nm z-shift

Figure 4.15: AFM image of the indented holes prepared with the increasing parameter of z-shift (from left to right). All images have same scale.

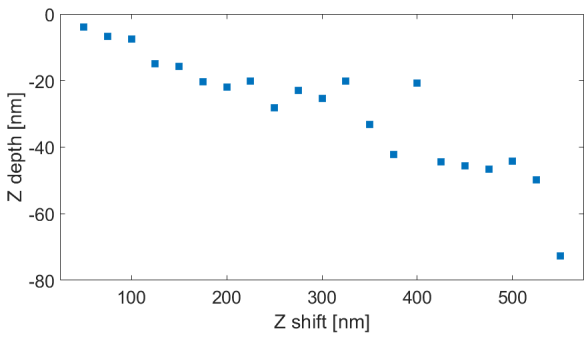

Figure 4.16: Depth of holes from fig. 4.15 and from further not displayed data. Depth determined by Gwydion from the AFM topography.

The holes are not visible under the DF microscope but we can make an AFM image of the area to observe the array (fig. 4.18). We can see that the programmed spacing in between the holes is not completely uniform, because the smallest step the machine can make did not match the programmed spacing.

Afterwards the samples were etched by oxygen RIE and the gold was deposited. But after the lift off no structure was found on the sample. This might be explained in several ways. The holes were not deep enough in order to etch the PMMA; or we did not etch the PMMA deep enough and the resulting structure was lifted off with the remaining polymer.

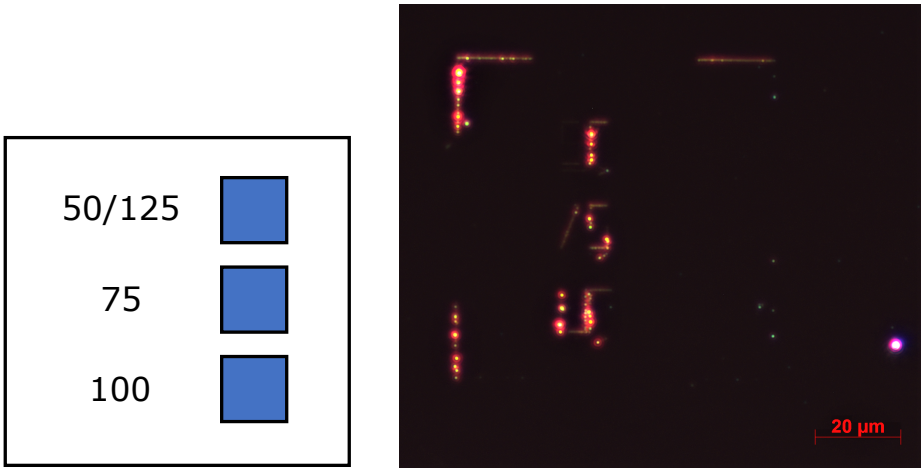

Figure 4.17: The AFM indentation protocol with annotations. Left: The scheme of the AFM indentation protocol. Three sets of holes with annotation of different z shift could be produced at one place. The blue square shows the area where the holes are indented. Right: DF image of indented holes with annotations (50, 75, 100), the holes (right from the annotation) are not visible in the DF microscope.

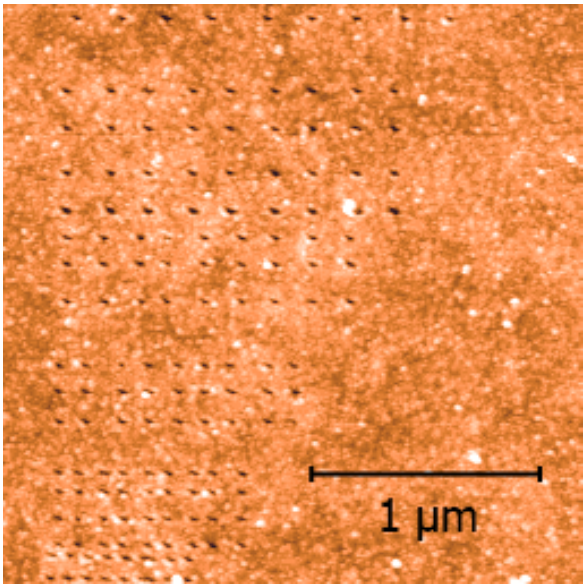

Figure 4.18: AFM image of indented holes for the z shift of 100 nm. The top row with 150 nm spacing up to the bottom row with 75 nm spacing.

In possible further development of this technique, the step size and other important parameters of the AFM machines should be considered. The current procedure is working with the program and machine Nanoscope from company Bruker and is not necessarily implementable to other machines or software. The AFM lithography procedure also takes longer times (in range of hours for one sample) than deposition for other colloid mask methods (hour for whole batch of 12 samples). Such a times are in same range as

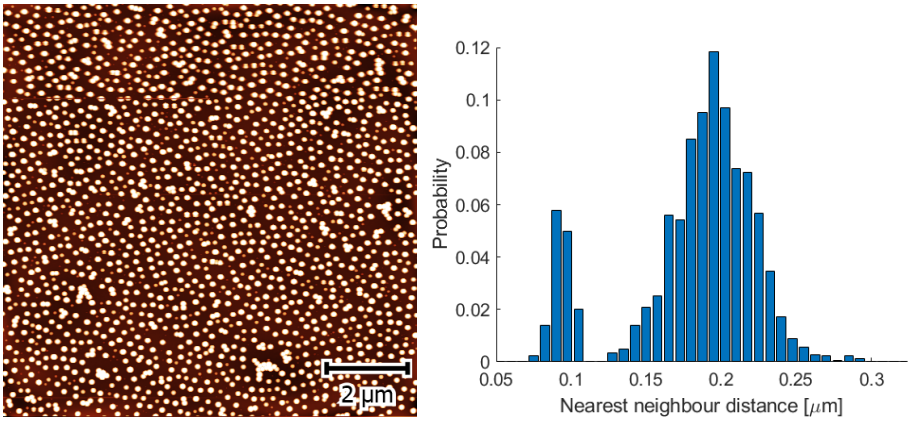

Figure 4.19: The resulting structure of colloid lithography. Left: AFM image of resulting structure from the colloid mask lithography. Right: The NND analysis of the data shown 15 % aggregation and density of 18 beads/μm^2

for the electron beam lithography. The precision of this method is much lower than of the electron beam lithography as it depends on the tip size and many other procedure and machine parameters. From this reason we would not recommend further development of this method for neither large scale nanoparticles manufacture as well as study of precise coupled plasmonic systems.

4.7 Colloid mask lithography

The process of colloid mask lithography underwent a lot of changes during the experimental process. First we used the pre-made substrates with 3 nm titanium and 20 nm gold with varnish. The samples were cleaned and the 100 nm polystyrene beads were homogeneously distributed over the whole sample. The gold layer was etched with argon etching. Parameters for argon etching were: voltage 400 V, power source 150 W, etching angle 90° for 15 seconds and 80° for 20 seconds. The resulting structure can be seen in fig. 4.19. The analysis shown homogeneous distribution with 15 % aggregation and 18 beads/μm^2 which is a noticeably improved result concerning the optimization of parameters from table 4.1. After the etching, the rest of the PS beads should be removed by the ultrasound bath in acetone or tape stripping. This was not possible due to the melting and interlinking of the polymer during the etching process, making it more resilient and adhesive to the disc. The structure from fig. 4.19 was therefore covered by the polystyrene cap. The cross-section of one particle from the AFM topography can be seen in fig. 4.20. At the cut we can also see that the diameter of the resulting structure is around 140 nm (approximated by Gwydion [70] grain analysis using the diameter of the equivalent circle). The possible use of such structure for sensing is impaired by the significantly smaller area of gold exposed to the specimen. This cap can be prevented by the use of silica glass beads and finalizing the structure with tape stripping.

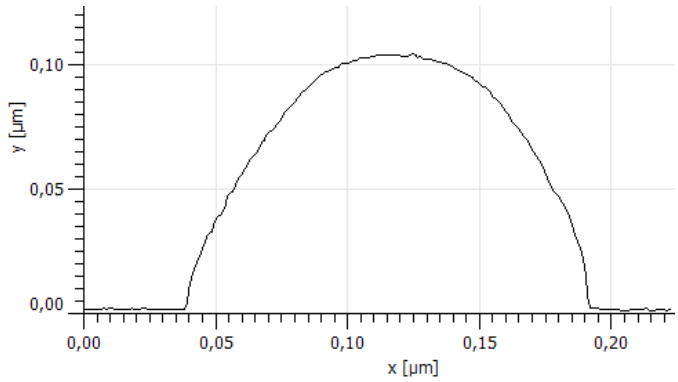

Figure 4.20: The profile of cap covering the golden nanodisc. Nanodisc has height of 20 nm, molten polystyrene bead is forming 80 nm high cap. The diameter of the disc was estimated by Gwydion to 140 nm.

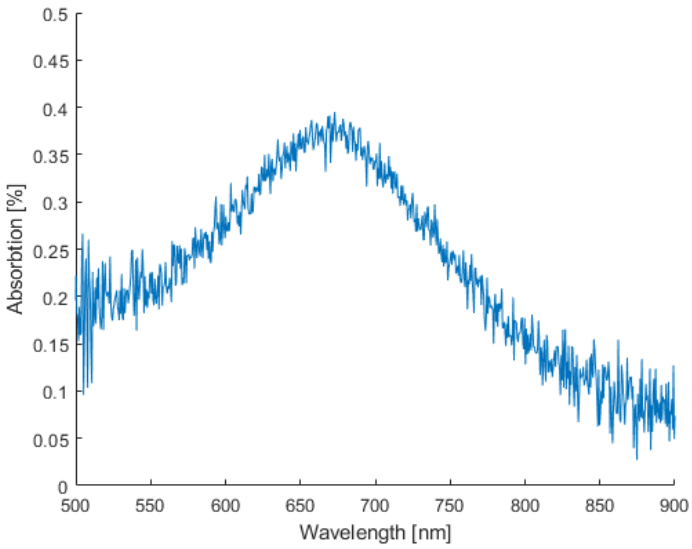

Figure 4.21: Optical absorption of the single gold nanodisc covered by the polystyrene cap left after the etching. The raw spectral data were taken in setup for dark field microscopy (single particle measurement) with spectrometer.

The single particle absorption spectra of the polystyrene caped disc is shown in fig. 4.21. The absorption was calculated according to the formula 2.2 on page 19. All of the quantities were obtained from measurements. We can see that the centre of the peak is in the red spectral region around 670 nm. The spectra has a large noise to signal ratio, which is caused by low intensity in the single particle measurement. For the measurement in microfluidics we can expect a further red shift in the spectra due to higher refraction index of water which is usually the medium containing the protein specimen.

To prevent the formation of the cap, we used silica beads in further

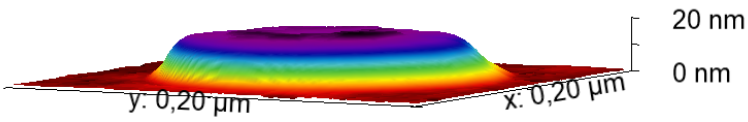

Figure 4.22: The AFM topography of the disc created by the colloid mask lithography. The 100 nm silica beads were used as a mask on 20 nm gold layer, resulting in disc with the diameter of 120 nm and the height of 20 nm.

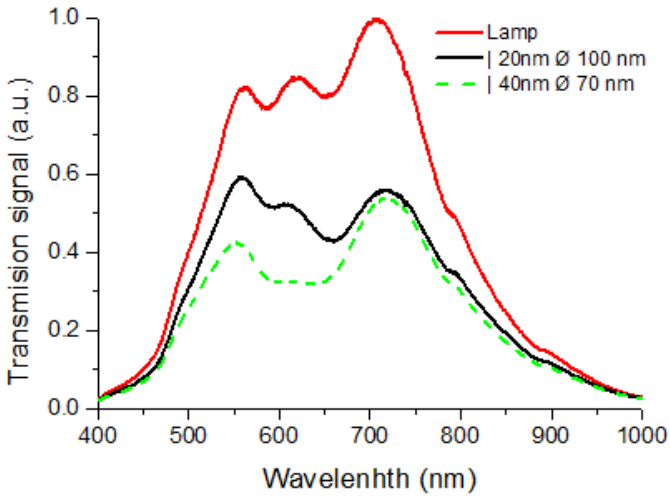

Figure 4.23: The transmission measurement data necessary to calculate the absorption of the plasmonic nanostructures. The lamp reference spectra and the transmission spectra of the disc structures with mask sizes: diameter 100 nm and thickness 20 nm and diameter of 70 nm and thickness of 40 nm.

experiments. The silicon oxide does not melt during the etching process and can be easily stripped by the adhesive tape. The nanostructures for further sensing were produced in two sizes:

- Diameter of 100 nm, height of 20 nm (100/20)
- Diameter of 70 nm, height of 40 nm (70/40)

Another combinations of the diameter and the ratio could be produced via the same procedure, varying only the thickness of the gold layer and the particle size. The disc structure (100/20) made with silica beads can be seen in fig. 4.22. The discs created by this method is 20 nm smaller in diameter then the one utilizing the polystyrene beads (the same size and the same procedure parameters were used). This effect is to be assigned to the melting of the polystyrene during the etching process so it effectively creates a larger mask. The disc created by silica beads are now suitable for measurements in the microfluidic or other chamber. The source for the transmission setup was a halogen lamp. Before the measurement the parameters of the lamp and spectrometer were optimized to get the highest possible signal. The spectra of the lamp (fig. 4.23) covering whole spectral region in which the discs

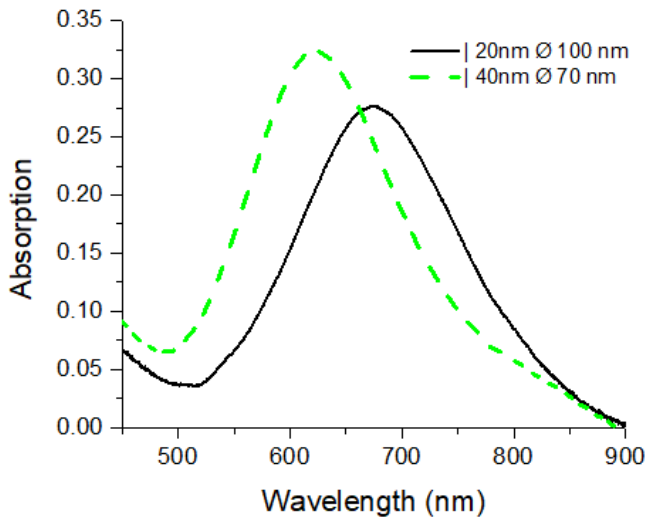

Figure 4.24: Absorption of two types of disc nanostructures. The black solid line corresponds to the disc created using 100 nm beads and 20 nm of gold. The green dashed line corresponds to the 70 nm beads and 40 nm gold layer.

can be tuned. The transmission measurements of the two disk variants are depicted in the same graph (fig. 4.23). The data was used to calculate the absorption according to the formula 2.2 on page 19. The dark current of the camera was interpolated from the spectra values out of the spectral range of the lamp. The resulting absorptions are shown in fig. 4.24. In the further microfluidic measurement we utilize the fit of the absorption peak and track the shift of its centroid [46].

4.7.1 Stability of the structure

One of the motivations to create the plasmonic nanostructures by the mask method was to increase the stability and reusability of the sensor chips. The stability against mechanical wear is compared to the chips with plasmonic particles dispersed from the colloid, a method currently used for localised plasmon sensing. The mechanical wear of the chip is usually caused by the sealing of the microfluidic chambers, cleaning of the chip between measurements and the flow of the liquid in the chamber itself. For an example case, a chip of each kind underwent 5 times tape stripping, simulating the wear caused by removing the sealing from the chip. The example case can be seen in fig. 4.25. The chip Q1 (left) contains 60 nm golden plasmonic nanospheres deposited from colloid with plasmonic peak around 540 nm. The second chip is the 100/20 disc structure prepared by colloid mask lithography. It is visible by bare eye, that the structure from the Q1 chip is almost completely removed by the process. It does not further provide sufficient signal for the measurements. The 100/20 lithography structure is not noticeably damaged. After the process the absorption of the chip is decreasing only in order of percent by each use; therefore, it can be used multiple times.

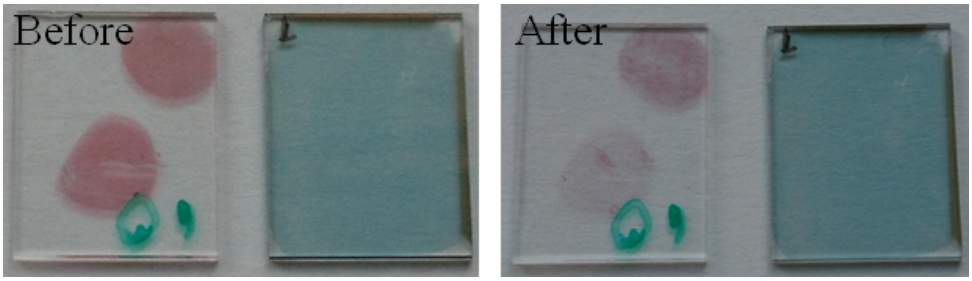

Figure 4.25: The picture of the chips used for localized plasmon resonance sensing. "Before" and "after" images show the example of mechanical wear of the chip by sealing of the microfluidic chamber simulated by tape stripping process. The Q1 chip with golden nanoparticles deposited from colloid and the 100/20 structure produced by the colloid mask lithography.

Table 4.4: The summary of fitted centre values of the simulated extinction cross-sections (S) and measured absorption (M) peaks. The mixed environment estimation value (E) is originating from the single environment simulations assuming symmetry of the model.

Disc	Centre of the absorption peak [nm]						
	S. air	S. water	S. glass	E. air/glass	E. wat/glass	M. air/glass	M. wat/glass
100/20	579	690	752	665	721	674	714
70/40	528	583	-	-	-	623	-

The final protocol for producing nanodics by colloid mask lithography can be found in appendix A.2 on page 68

4.7.2 Simulation comparison

Before we move to the measurements in microfluidic chamber in real time, we shall examine what is the expected response of the structures calculated by the simulations. The extinction cross-section of golden disc model (as introduced in section 3.4 on page 31) was calculated for two different media; air with $n = 1$ and water with $n = 1.33$. Two possible sizes of the disc (100/20 and 70/40) were simulated (fig. 4.26). The most important is the red shift of the resonant peak due to the change of the refraction index (generally the permittivity) which will allow later calculation of the sensitivity of the disk to the refraction index. We may notice that the disc 70/40 has approximately three times lower extinction for both environments. This is caused by the size of the disc. This effect is levelled in the measurements due to the higher densities of the smaller discs assembly[7].

For the simulation, the disc is fully surrounded by the media, which is only an approximation of the real structure. In reality the structure is always in contact with the glass substrate. Assuming that the glass has $n = 1.5$,

[7]The homogeneously distributed assemblies of the 70/40 discs were showing densities around 40 beads/μm^2 and aggregations up to 10%.

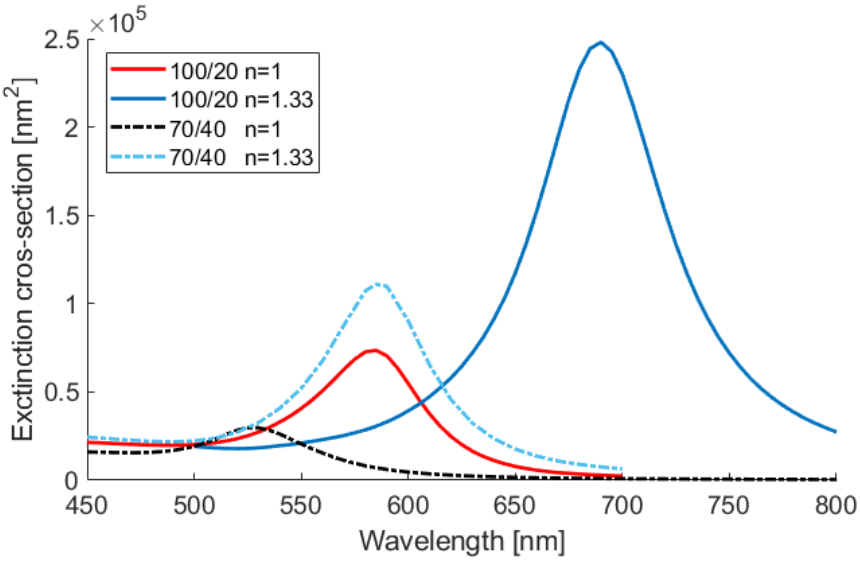

Figure 4.26: The simulated extinction cross-sections of discs with sizes 100/20 (solid) and 70/40 (dashed). The simulation was performed in the two environments with constant refraction index; air $n = 1$ and water $n = 1.33$. The simulation shows red shift for the media with higher value of n.

Table 4.5: The sensitivities for the simulation of the 100/20 discs fully surrounded by one media.

Media	air − water	air − glass	water − glass
Sensitivity [nm/RIU]	336	346	364

we can expect red shift of the structure resonation peak. The summary of simulated (S) and measured (M) structure resonance peak is in table 4.4. For the disc 100/20, the simulation in purely glass environment was additionally calculated. Using the additional information, we can calculate a closer approximation of the real disk on the glass wafer using the symmetrized approximation and estimate that resonant peak will be at average of the calculated values (estimate values noted by E.). This estimate gives us only the position of the peak, information about the other parameters and shape of the absorption profile is not accessible.

From the simulation we can additionally calculate the sensitivity of the disc. The sensitivity is measured in nanometres per refractive index unit (nm/RIU) and is calculated from the positions of the centre of the peak R in the different media

$$S = \frac{R_1 - R_2}{n_1 - n_2} = \frac{\Delta R}{\Delta n}. \tag{4.2}$$

For the 100/20 disc simulations, we can calculate sensitivities for different surrounding media. The sensitivities for the disc fully surrounded by one medium are in the table 4.5. The values are comparable within the accuracy of the model which shows the linearity of the sensitivity in the region of exam-

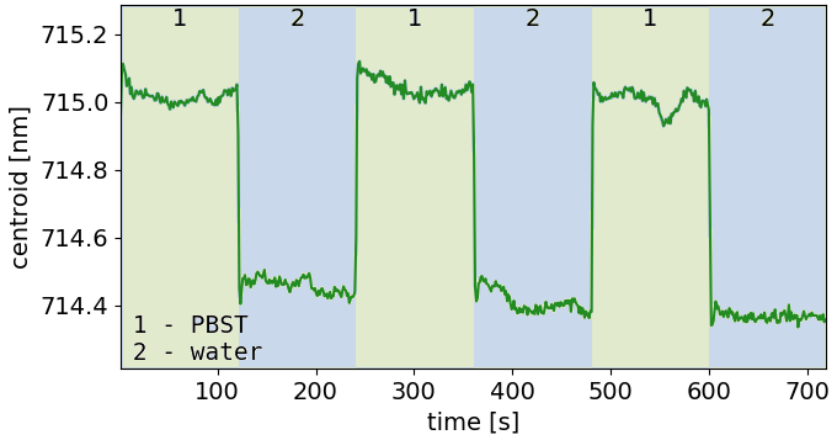

Figure 4.27: Example of calibration measurement performed with the 100/20 disc structure. The mili-Q water and PBST buffer with $\Delta n = 0.0017$ were pumped into the system in 120 seconds intervals. Structure sensitivity was estimated to 362 nm/RIU.

ined n values. For the 70/40 disc the sensitivity is 167 nm/RIU. Calculating the sensitivity from the measured data we need to take into consideration that only part of the disc is influenced by the Δn (three media influence the disc). The sensitivity calculated by the eq. 4.2 is 121 nm/RIU. This result is not correct due to the three media system sensitivity not being possible to approximate by one media sensitivity for large Δn.

4.8 Microfluidic calibration measurement

The next step towards the ability to perform protein measurement with the disc structures is to test them in the microfluidic chamber system. To ensure that the structure is suitable for the protein measurements, series of calibration measurements is performed and stability of the signal tested. Calibration is than performed before every experiment to ensure the correct scaling of ΔR to Δn. The calibration process uses two fluids of known constant refraction index (measured on refractometer right before the calibration). For the calibration purposes are generally used the same liquids as we would in the following experiment. Our test was performed with mili-Q water used to flush and clean the chamber and PBST (Phosphate Buffered Saline) buffer which is widely used for the protein measurements. The microfluidic chamber measurement works with live data processing to show the current position of the peak centre (centroid) to provide overview over the current situation. The pump than pumps the desired liquids to the chamber. The speed of pumping and source of the liquid are preset by the user in the measurement settings (form of a script). The data are than saved in raw spectral form allowing post-processing and further data analysis. The example of the calibration performed with the disc structure (100/20) is shown in fig. 4.27. The PBST

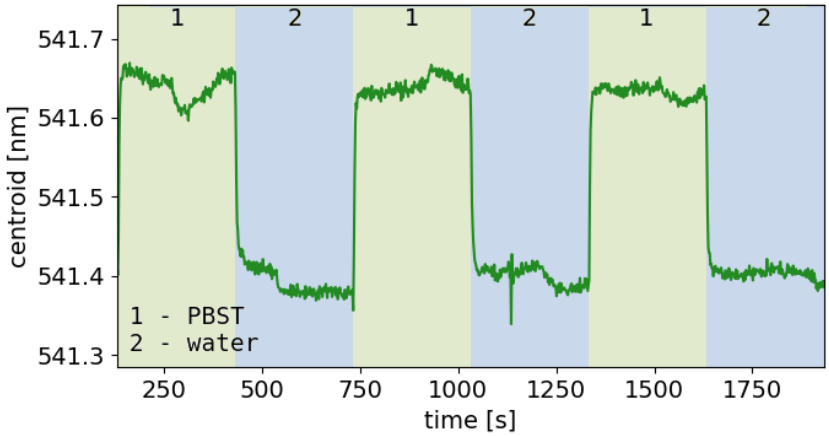

Figure 4.28: The calibration measurement example performed with the 60 nm spheres structure. The mili-Q water and PBST buffer with $\Delta n = 0.0017$ were pumped into the system in 360 seconds intervals. Structure sensitivity was estimated to 139 nm/RIU.

Table 4.6: The summary and comparison of measured parameters of two sample types. The λ - wavelength is the approximate position of the absorption peak. Sensitivity span is estimated taking in consideration multiple measurement with the same structure. The noise is calculated as deviation from mean value of static measurement. The value of error is calculated from noise divided by averaged sensitivity.

Sample	λ [nm]	Sens. [nm/RIU]	Noise [nm]	Error [RIU]
60 nm Spheres	541	130−140	0.008	$6 \cdot 10^{-5}$
100/20 Discs	714	360−370	0.024	$7 \cdot 10^{-5}$

buffer with $n_1 = 1.3343$ and mili-Q water with $n_1 = 1.3326$ were pumped in 120 seconds intervals to the chamber. The Sensitivity is then calculated using mean values of signal for different refraction indices. The sensitivity was determined to be 362 nm/RIU for this measurement. This value corresponds to the estimate (352 nm/RIU) based on the simulated data. The value is also noticeably higher than the estimate from the measurement based on large Δn (121 nm/RIU) which confirms that the sensitivity for the three media system cannot be approximated linearly for large Δn. To compare the quality of the disc structures to the usually used particles (same as the comparison of mechanical stability) equivalent calibration was performed (fig. 4.28). The signal and sensitivity are the only parameters accessible during the measurement. To obtain more information about the structure, we need to examine the noise of the measurement. The summary made from analysis of multiple measurements can be seen in table 4.6. The disc structures were showing overall higher values of sensitivity as well as noise. The noise is calculated from measurement with no flow in the chamber. The important value to compare is the order of error in RIU (noise/sensitivity), which was

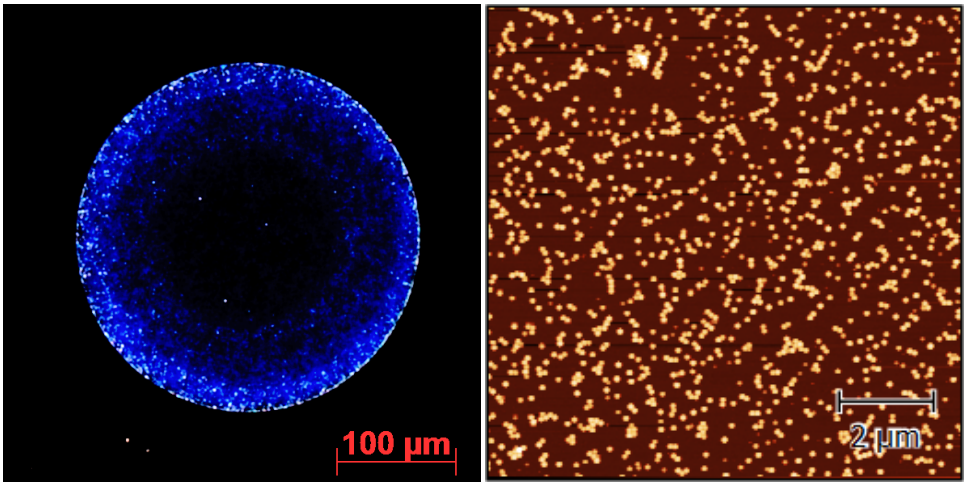

Figure 4.29: Structure with beads deposited by method of microarray plotting. The dark field microscopy image (left) is showing one of the droplets made with solution with concentration of 0.05% wt of silica beads. The AFM image (right) shows the distribution of the beads in the middle of the spot.

for both types of structures 10^{-5} RIU. This value is comparable with other published SPR and LSPR measurements, which can vary from 10^{-3} to 10^{-6} [see 76]. With this knowledge we can safely say that the structures prepared by colloid mask lithography are generally as good or better than the previous methods; providing the same sensitivity on more mechanically stable chips with possibility of multiple use.

4.9 Microarray plotting

We have already shown that the colloid mask lithography can produce chips suitable for microfluidics measurements. So far we were able to create structures on the whole area of the chip and utilize them for one channel microfluidic measurement. The method of microarray plotting can be combined with the colloid mask lithography. This combination brings more stable sensors for the multichannel measurements. Two methods how to combine the methods were proposed in section 3.1.5 on page 27. Both of these methods were tested to create such a microarray. The first method utilizes the direct dispersion of the mask (silica) particles. A series of samples with different concentrations of colloid were plotted and the parameters important for the method. For the experiment, we used silica spheres on Ti/Au substrate. The concentrations of the silica bead colloid were varying from 0.5% wt to 0.005% wt. After deposition, the samples were observed by dark field microscopy and AFM. The structure obtained by the concentration 0.05% wt (fig. 4.29) shows the test structure with the best parameters. From the dark field image, we can notice the gradient in intensity on an optical scale caused by the coffee ring effect. This continual increase in the structure density is not a problem for the sensing as long as the aggregation on the edges does not interfere with

the main signal in the same way as it could interfere in the case of the fully covered chips. The AFM picture then shows the distribution of the particle in the middle of the spot. The level of aggregation and density has changed between the different test measurements (results shown in section A.3 on page 69). We can see that many parameters will need to be optimized to obtain structures suitable as sensors. Those parameters are same as for all of the microarray plotting techniques.

To avoid the dispersion of the mask we can use the second method with additional etching step. This way finished structure made by colloid mask lithography is spotted by glue resist and etched again. The resist was supposed to be removed from the structure by acetone isopropanol bath. This step did not work most likely due to the cross-linking of the polymer strands. The removal by acid or stronger solvent will be required. With the preliminary results, we can say that the mask lithography will be possible to be performed together with the microarray plotting. The optimization of the parameters is nevertheless beyond the scope of this work and will be left for the further research.

4.10 Protein measurements

To be able to simulate the reactions of the plasmonic sensor and to perform microfluidic measurement with the protein, we must measure and calculate the spectrum and concentration of the protein. The starting water solution of the protein (horse myoglobin) had an unknown concentration. The measurement was performed with spectrometer NanoDrop using the method based on the ultra violet absorbance (280 nm) of amino acids. To calculate the concentration we need to measure the extinction at 280 nm (A), the lenght of the optical path l and the extinction coefficient ϵ. The extinction coefficient is calculated by ExPASy [77] using the sequence of the protein. The sequence was taken from the database UniProt [78]. The concentration is than equal to

$$c = \frac{A}{\epsilon l}.$$

The protein was than diluted to have 0.002 g/ml for further measurement in cuvette.

For the absorbance of the myoglobin in the different states we need to do two sets of measurement to have all the important spectra. This is caused by the necessity of the removal of the dithionite salt to achieve the OMb. The first series consists of three stages (blue) and the second one contains one additional stage (red):

- metMb state of starting solution
- DOMb state after application of dithionite salt
- OMb state after separating the protein from salt
- COMb state after introducing the CO gas.

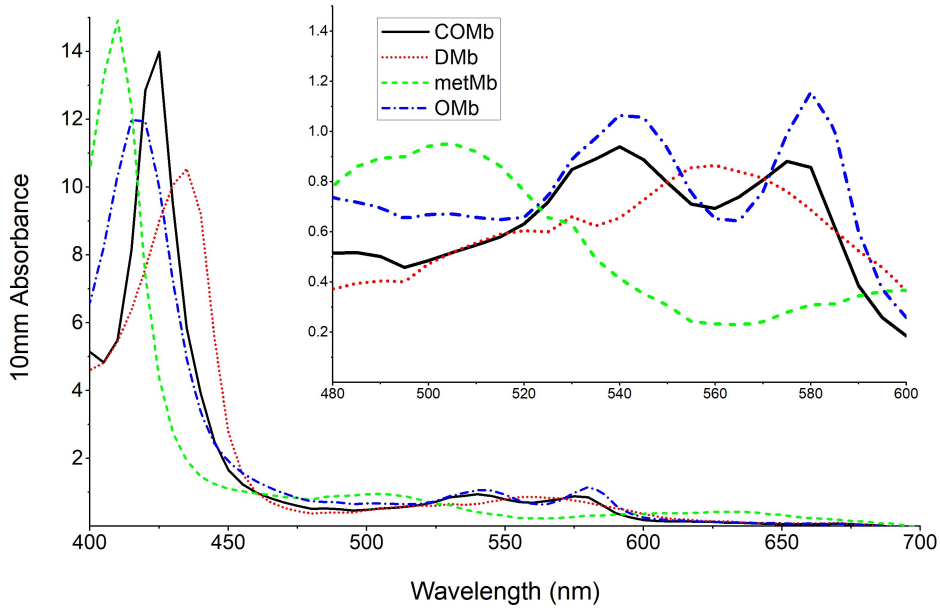

Figure 4.30: The absorbance of all stages of the myoglobin. The data is used for calculating the change in the permittivity relevant for the LSPR sensing.

In the first process the dithionite salt is always present and reacts with the free oxygen molecules, preventing the formation of OMb state. The separation of the protein from the salt is done by a gel chromatography. This step changes the concentration of the protein solution to an unknown value. The data from the COMb state are than used to correct the intensity values to the same scale as the previous set. The measured data from all of the states (fig. 4.30) can now be used as a template for the model of absorption index used for the calculation of the permittivity for the COMSOL modelling.

4.11 Protein simulations

The last step in simulating the sensor is to combine the possibility of modelling the disc in the chosen environment together with the measured data from the protein. The 5 nm layer of protein is modelled around the disc. The permittivity of this layer is based on κ calculated from the protein absorbance and n calculated via Kramers-Kronig (K-K) relations.

4.11.1 Absorption and refraction indices

The protein absorbance $A(\lambda)$ was gathered on the optical path $l = 10$ mm. Using the definition of absorbance

$$A(\lambda) = \alpha(\lambda) l \log(e) \tag{4.3}$$

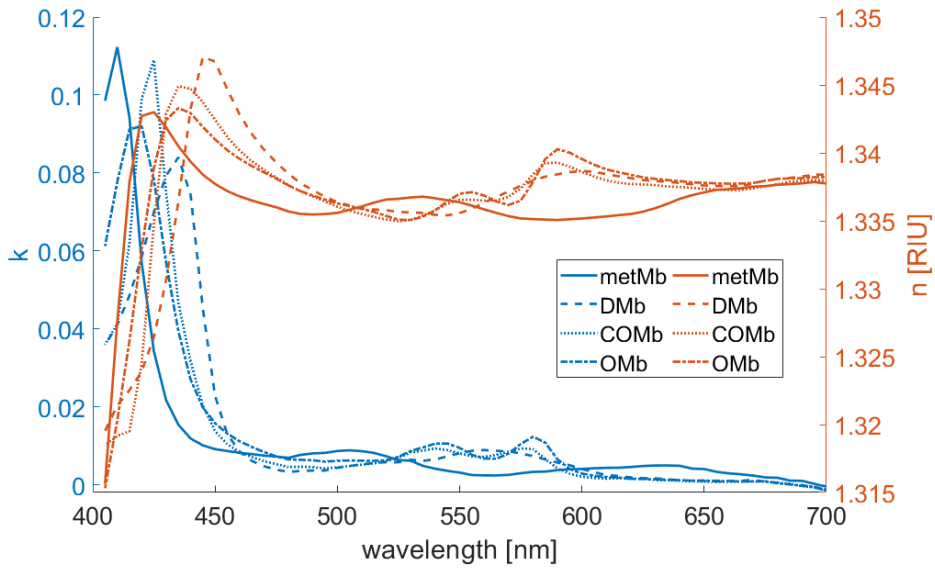

Figure 4.31: The absorption index κ (noted as k) and refraction index n used in the simulations with concentration of 10 g/ml.

we can write absorption index

$$\kappa(\lambda) = \frac{\alpha(\lambda) \cdot \lambda}{4\pi} = \frac{A(\lambda) \cdot \lambda}{4\pi l \log(e)} \tag{4.4}$$

where α is the coefficient of absorption from the Lambert-Beer law and λ is wavelength of the light in the surrounding media. The absorption index is calculated using the measured dataset (wavelength, absorbance) directly, with chosen concentration of the protein to be either 1 g/ml or 10 g/ml. This concentration is not the concentration of the solution pumped into the microfluidic chamber, but a local concentration of the protein in the 5 nm layer on the disc. Considering the the protein is globular with an approximate size of 5 nm, we can say that even if its closely packed, the local concentration cannot exceed a concentration of 3 g/ml. The choice of the simulated value of 1 g/ml comes from the idea that the protein can never be packed closely on the surface. The second value of 10 g/ml is then chosen to show insufficiency of the protein absorption even for larger (not experimentally possible) concentrations. The refractive index n is then calculated as the constant refractive index of the media (water) plus refractive index calculated from κ via the K-K relations (fig. 4.31 and fig. A.5 on page 70). Note that the refractive refraction index does not change linearly with the absorption index due to the form of K-K relations (equation 3.3 on page 29). From the n and κ we can calculate the effective refraction index as $n_{eff} = \sqrt{\varepsilon} = \sqrt{n^2 + \kappa^2}$. The differences between n_{eff} of the different myoglobine states do not exceed 10^{-3} for 10 g/ml and 10^{-5} for 1 g/ml which is on the sensing limit for media with constant absorption index.

4.11.2 Extinction

The simulation for 70/40 nm disc with 5 nm layer of protein were done for three of the protein states. The spectra are than fitted according to theory published in [46]. The peak centroid is calculated based on a high order polynomial fit of the peak. The fitted x range is determined by the span parameter [nm] (example shown in fig. A.4 on page 70). The fits were performed for both concentrations for 4 values of the span. For the concentration of 1 g/ml none of the difference between the peak centroids exceeds 0.024 nm (noise value determined by an analysis of the experimental measurements of the disc) therefore we cannot expect detection of any change in the state of the protein. All the data are shown in table A.1 on page 71. The results for the higher concentration of 10 g/ml are showing that in higher concentrations the difference between metMb and COMb or DMb could be observable by the plasmonic sensor. The plasmonic sensor cannot rely on sensing the difference between the COMb and DMb state which did not exceed 0.01 nm (half of the estimated noise level). We can expect that the OMb state (not calculated) will not be observable as well due to smaller difference in the refraction index from COMb state, than is between the COMb and DMb states. All the data are shown in table A.2 on page 71.

Conclusions

The work was devoted to the description and manufacturing of the structures with a plasmon resonance. It provides theoretical insight to plasmons and plasmons-polaritons on planar interfaces as well as an introduction to the phenomena of localized plasmon resonance. Several colloid and non-colloid mask methods for production of LSPR nanodiscs were suggested and tested. The design of a CO sensor was proposed; utilizing the chips with the LSPR structure of golden nanodiscs and protein myoglobin. The main topic of the experimental work was the creation, characterization, and simulation of a plasmonic nanostructure created by mask methods. Additionally, the work contains the measurements and simulations for the proposed CO sensor.

For the colloid mask methods, we optimized the homogeneous distribution of particles; the parameters were scanned and additional procedure steps added. As a result, a work protocol was created for reproducible results. For all the methods (colloid mask, inverse colloid mask, hole-mask, and AFM mask) we scanned and tested important parameters. The hole and AFM mask lithographies did not result in active plasmonic structures. The improvement to the critical procedure step is proposed to be integrated in the future research of those methods. The colloid and inverse colloid mask lithography methods led to active plasmonic structures. The structures were spectrally characterized. The inverse mask lithography resulted in a structure with high absorption offset and a broad spectral peak. The colloid mask lithography structures (nanodiscs) were reproducible and had well-defined absorption peak. The absorption maxima were also in correspondence with the simulations.

The nanodiscs were created in two sizes 100 nm diameter with a thickness 20 nm and 70 nm diameter with thickness 40 nm. The sensitivity of the 100 nm disc structure was calculated and measured in the microfluidic chamber to be approximately 360 nm/RIU. The noise in the microfluidic measurement is 0.024 nm resulting in the detection limit $\Delta n = 7 \cdot 10^{-5}$ RIU. This result together with the proven mechanical stability of the chips makes them a suitable platform for the LSPR measurements. The method is together with the microarray spotting adaptable for multichannel sensorics.

The sensor for CO was first tested in silico. The simulations of the 70 nm disc with protein layer show, that the protein change in the Q-band absorbance

for different protein states (in the spectral region between 500-700 nm) is not sufficient enough to provide a significant shift of the absorption peak (significant considering the noise level). The conclusion is that the crucial step of CO bonding is not observable by the sensor as proposed.

To summarize, the protocol with optimized parameters, leading to reproducible LSPR nanodisc structure was created. The structures are suitable for the LSPR microfluidic chamber measurement with the possibility to be cleaned and used multiple times. The simulations have shown that such nanodisc structures are not a suitable platform to combine with Q-band absorption change of myoglobin protein to sense carbon monoxide.

Chapter A

Apendix

A.1 Preparation of sample substrates

Due to using multiple techniques for acquiring structures, it was necessary to treat substrates for each procedure differently. For the research of distributions in homogeneous assembly, basic cover glass in dimensions 1.8 × 1.8 cm were used.
Cleaning procedure steps:

- 10 minutes ultrasonic bath
  - Acetone
  - 50% Acetone 50% Ethanol mixture
  - Ethanol
  - Mili-Q water
- Mili-Q water rinse
- Drying by N_2 stream

Transitions between different cleaning solutions were wet to wet transfers.

More complicated methods requiring PMMA (poly(methyl metakrylate) fig. A.1) layer or gold deposition were first prepared in clean rooms. Three types of substrates were produced this way, PMMA layer only, PMMA + gold layer and gold layer only. Large wafers were deposited at once, therefore for the cutting of the wafer into small substrates (16 × 12.5mm), application of protecting layer of varnish was necessary.
Procedures in clean rooms (PMMA substrates):

- Cleaning
- Spin coating
- Baking at 200°C for 10 minutes
- Optional vapour deposition of 3 nm Ti + 20 nm Au layer
- Protective varnish deposition

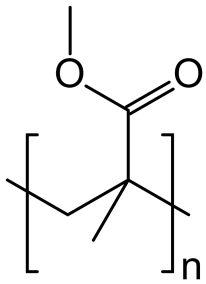

Figure A.1: Skeletal formula of the poly(methyl metakrylate) repeating unit $(C_5O_2H_8)_n$.

- Cutting

Spin coating speed was 3000 turns per minute with the resulting layer thickness 170 nm. Used resist was Copolymer PMMA/MA 33% as E-Beam Resist Series AR-P 617 in 1-methoxy-2-propanol. Layer of 2.2 μm was baked at 80°C for 30 minutes.
Protective layer removal:

- 5 minutes ultrasonic bath
  - Acetone
  - Isopropanol
  - Mili-Q water
- Mili-Q water rinse
- Drying by N_2 stream

After this treatment the layers were used as substrates for hole-mask lithography (without gold) and AFM mask lithography (with gold).

The substrates for the colloid mask lithography did not require further cleaning after deposition in clean rooms.
Procedures in clean rooms:

- Cleaning
- 4 nm Ti vapour deposition
- 20 nm Au vapour deposition

All the substrates used in methods requiring deposition of homogeneously distributed nanoparticles proceeded to further treatment in ozone cleaner. The substrates were exposed to O_3 plasma in low power plasma cleaner (17W) for duration of 10 minutes in order to negatively charge the surface. Substrate were than immediately 0.2 wt% PDDA (Poly diallyldimethylammonium chloride depicted in fig. A.2) polyelectrolyte solution in water was applied

for 15 minutes. Substrates were rinsed and stored[1] with Mili-Q water and dried by N_2 stream before the bead deposition.

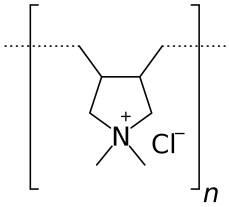

Figure A.2: Skeletal formula of Polydiallyldimethylammonium chloride repeating unit $(C_8H_{16}NCl)_n$.

[1]By storing we mean times maximally up to half an hour while the other procedures, chip deposition was done.

A.2 Protocol

The substrates pre-preparation:

- clean 0.7mm Boro glass chips
- evaporate 4 nm Ti
- evaporate 20(40) nm Au.

The substrates can be stored after this step.

The substrates preparation:

- 10 minutes ozone cleaner treatment
- 15 minutes in 0.2wt% PDDA solution in water
- store in water before deposition of beads.

Only temporary storage before deposition.

Beads deposition:

- Concentration of 0.05 wt% for 100 nm Sio2 beads (COOH surface charge)
- Concentration of 0.025wt% for 70 nm SiO2 beads (COOH surface charge)
- two minutes deposition time
- shaking during deposition
- properly rinsing after deposition − washing all non-attached beads from the surface to avoid coffee ring affect
- Drying under N_2 stream.

Argon etching parameters:

- voltage 400V
- power source 150 W
- 15 seconds 90° angle to surface
- 20 seconds 80° anfle to surface.

Tape stripping by the Nitto scandinavia tape SWT-10, repeat at least 5 times. Recommended to do just before first use to avoid contamination of the structure.

A.3 Microarray plotting

The summary of the figures for the microarray plotting. The parameters to optimize in further research: concentration of beads, droplet volume, humidity in the instrument, distance of micropipette from the sample, charging of the sample surface and others.

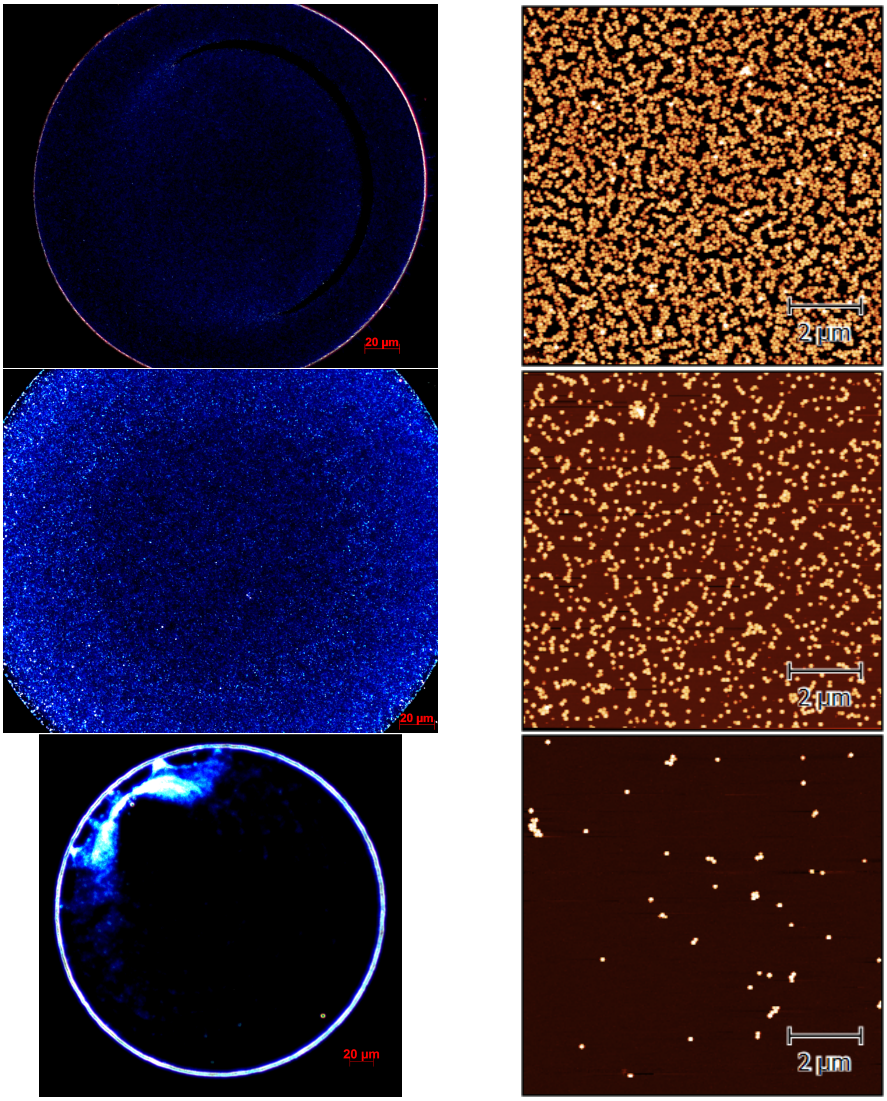

Figure A.3: Structure with beads deposited by method of microarray plotting. The dark field microscopy image (left) is showing one of the droplets made with solution with concentration of: 0.5% wt top, 0.05% wt middle and 0.005% wt bottom of silica beads. The AFM image (right) shows distribution of the beads in the middle of the spot. The intensities in the dark field image is not to scale due to the scaling to maximal intensity.

A.4 Protein simulation

Additional figures and tables for the protein simulations section.

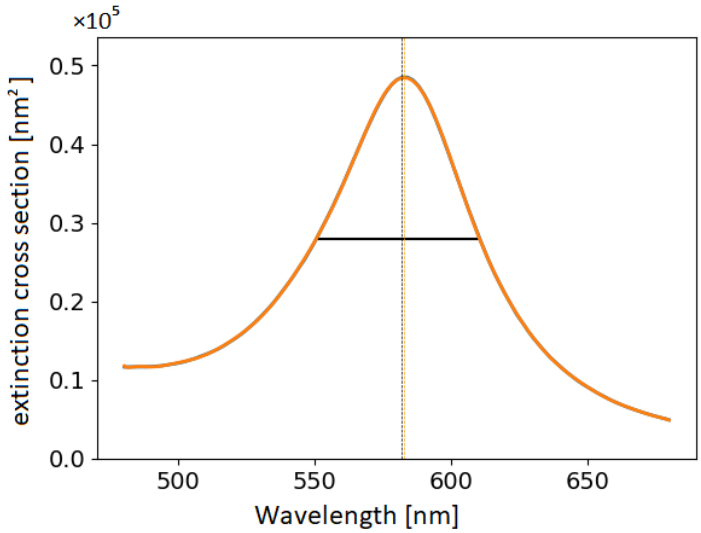

Figure A.4: The extinction cross-section of the disc model with DMb protein layer. The data line (blue) is overlaid by the fit (orange). The horizontal back lines shows the span for the centroid calculation. The vertical line then calculated position of the centroid.

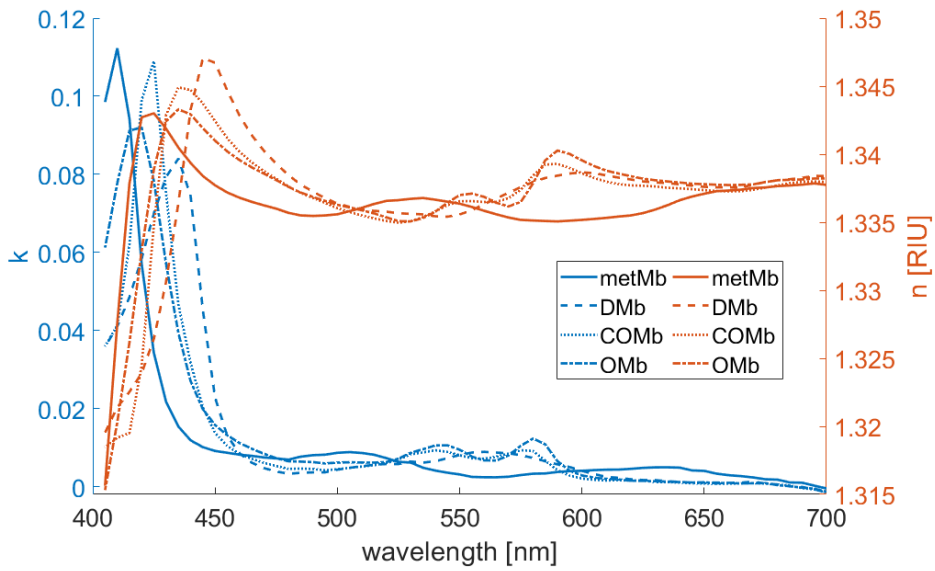

Figure A.5: The absorption index κ (noted as k) and refraction index n used in the simulations with concentration of 1 g/ml.

Table A.1: The values of peak centroids for span between 60 - 120 nm for three of the states of the protein and the corresponding differences in between the different states position for the protein concentration of 1 g/ml.

1 g/ml - Peak centroids [nm]

span	metMb	DMb	COMb
120	578.9549	578.9688	578.973
100	579.8007	579.8155	579.8054
80	580.5859	580.6021	580.5879
60	581.3619	581.3801	581.3715

1 g/ml - Differences [Δnm]

span	CO-met	D-CO	D-met
120	0.018 122	−0.004 183	0.013 938
100	0.004 736	0.010 073	0.014 809
80	0.002 039	0.014 163	0.016 202
60	0.009 643	0.008 565	0.018 208

Table A.2: The values of peak centroids for span between 60 - 120 nm for three of the states of the protein and the corresponding differences in between the different states position for the protein concentration of 10 g/ml.

10 g/ml - Peak centroids [nm]

span	metMb	DMb	COMb
120	579.1292	579.2674	579.2579
100	579.9521	580.0994	580.0945
80	580.7246	580.8861	580.883
60	581.4944	581.6762	581.6773

10 g/ml - Differences [Δnm]

span	CO-met	D-CO	D-met
120	0.128 755	0.009 495	0.138 249
100	0.142 423	0.004 919	0.147 341
80	0.158 391	0.003 14	0.161 531
60	0.182 941	−0.001 15	0.181 789

A.5 Summary of used equipment

Following list comprehends mostly used instrumentation and software.

Table A.3: Summary of used software.

Software	Company	Specification
AxioVision	Carl Zeiss microscopy	Microcope software
Nanoscope 9	Bruker	AFM software
Matlab R2018a	MathWorks	Data analysis and simulations
Gwyddion	Open-source published in [70]	AFM data analysis software
COMSOL Multiphysics	COMSOL	Modelling software
WinSpec	Princeton instruments	Spectral measurement software
Fresnel simulace v.5	LKSoft	ATR analysis software
OriginPro 9	OriginLab	Data analysis and plotting
GenX	Open-source published in [74]	SAX data simulations and fitting

Table A.4: Summary of used instrumentation.

Instrument	Company	Specification
UV Ozone cleaner UVC-1014	Nanobioanalytics	Power 17 W, Imp. current 7000 mA
200G-plasma system, O_2 plasma stripper	Technic plasma GmbH (TePla)	Vacuum 0.6 mbar, O_2 pressure 1.6 mbar, power 380 W
Ulrtasound bath Bandelin	Sonorex	
Vibramax 100	Heidolph	300 rounds per minute
Vortex gene	Scientific industries Inc	
Nanoscope V	Bruker	Tapping/contact mode
PVD system RHVm42	HVD	Physical vapour deposition system
Tap 300 AL-G AFM tip	Budget sensors	300 kHz frequency, 40 mN force constant
Nano-Plotter 2.1	GeSiM	Microarray printer
AxioImager Z1m	Carl Zeiss microscopy	Microscope
AxioCam MRc5	Carl Zeiss microscopy	CCD
EC Epiplan 5x, 10x, 20x, 50x, 100x	Carl Zeiss microscopy	Objective
Spectra Pro 2300i	Princeton instruments	Spectrometer
PPS-0.1COOH Polystyrene beads	Kisker Biotech GmbH & Co. KG	Carboxylated 100 nm size polystyrene beads
SWT-10 tape	Nitto Scandinavia AB	Pressure sensitive acrylic-based adhesive tape

Bibliography

[1] Stefan A. Maier and Harry A. Atwater. Plasmonics: Localization and guiding of electromagnetic energy in metal/dielectric structures. *Journal of Applied Physics*, 98(1):1–10, 2005. ISSN 00218979. doi: 10.1063/1.1951057.

[2] Nina Jiang, Xiaolu Zhuo, and Jianfang Wang. Active Plasmonics: Principles, Structures, and Applications. *Chemical Reviews*, 118(6):3054–3099, 2018. ISSN 15206890. doi: 10.1021/acs.chemrev.7b00252.

[3] Jianji Yang, Harald Giessen, and Philippe Lalanne. Simple analytical expression for the peak-frequency shifts of plasmonic resonances for sensing. *Nano Letters*, 15(5):3439–3444, 2015. ISSN 15306992. doi: 10.1021/acs.nanolett.5b00771.

[4] Jack J. Mock, David R. Smith, and Sheldon Schultz. Local refractive index dependence of plasmon resonance spectra from individual nanoparticles. *Nano Letters*, 3(4):485–491, 2003. ISSN 15306984. doi: 10.1021/nl0340475.

[5] V. G. Kravets, A. V. Kabashin, W. L. Barnes, and A. N. Grigorenko. Plasmonic Surface Lattice Resonances: A Review of Properties and Applications. *Chemical Reviews*, 118(12):5912–5951, 2018. ISSN 15206890. doi: 10.1021/acs.chemrev.8b00243.

[6] Zhaojian Zhang, Junbo Yang, Xin He, Jingjing Zhang, Jie Huang, Dingbo Chen, and Yunxin Han. Plasmonic refractive index sensor with high figure of merit based on concentric-rings resonator. *Sensors (Switzerland)*, 18(1), 2018. ISSN 14248220. doi: 10.3390/s18010116.

[7] Jiří Homola, Ivo Koudela, and Sinclair S. Yee. Surface plasmon resonance sensors based on diffraction gratings and prism couplers: sensitivity comparison. *Sensors and Actuators, B: Chemical*, 54(1):16–24, 1999. ISSN 09254005. doi: 10.1016/S0925-4005(98)00322-0.

[8] Jeffrey N. Anker, W. Paige Hall, Olga Lyandres, Nilam C. Shah, Jing Zhao, and Richard P. Van Duyne. Biosensing with plasmonic nanosensors. In *Nanoscience and Technology: A Collection of Reviews*

from Nature Journals, volume 7, pages 308–319. Co-Published with Macmillan Publishers Ltd, UK, aug 2009. ISBN 9789814287005. doi: 10.1142/9789814287005_0032.

[9] Katherine A. Willets and Richard P. Van Duyne. Localized Surface Plasmon Resonance Spectroscopy and Sensing. *Annual Review of Physical Chemistry*, 58(1):267–297, 2007. ISSN 0066-426X. doi: 10.1146/annurev.physchem.58.032806.104607.

[10] Yoochan Hong, Yong Min Huh, Dae Sung Yoon, and Jaemoon Yang. Nanobiosensors based on localized surface plasmon resonance for biomarker detection. *Journal of Nanomaterials*, 2012(1):1–13, 2013. ISSN 16874110. doi: 10.1155/2012/759830.

[11] Joseph R. Lakowicz. Plasmonics in biology and plasmon-controlled fluorescence. *Plasmonics*, 1(1):5–33, 2006. ISSN 15571955. doi: 10.1007/s11468-005-9002-3.

[12] Juan Yguerabide and Evangelina E. Yguerabide. Light-scattering submicroscopic particles as highly fluorescent analogs and their use as tracer labels in clinical and biological applications II. Experimental characterization. *Analytical Biochemistry*, 262(2):157–176, 1998. ISSN 00032697. doi: 10.1006/abio.1998.2760.

[13] Andrea Csaki, Thomas Schneider, Janina Wirth, Norbert Jahr, Andrea Steinbrück, Ondrej Stranik, Frank Garwe, Robert Müller, and Wolfgang Fritzsche. Molecular plasmonics: light meets molecules at the nanoscale. *Philosophical Transactions of the Royal Society A: Mathematical, Physical and Engineering Sciences*, 369(1950):3483–3496, sep 2011. ISSN 1364-503X. doi: 10.1098/rsta.2011.0145.

[14] Yugang Sun and Younan Xia. Shape-controlled synthesis of gold and silver nanoparticles. *Science*, 298(5601):2176–2179, 2002. ISSN 00368075. doi: 10.1126/science.1077229.

[15] Stephan Link and Mostafa A. El-Sayed. Shape and size dependence of radiative, non-radiative and photothermal properties of gold nanocrystals. *International Reviews in Physical Chemistry*, 19(3):409–453, jul 2000. ISSN 0144-235X. doi: 10.1080/01442350050034180.

[16] Andrea Csáki, Matthias Thiele, Jacqueline Jatschka, André Dathe, David Zopf, Ondrej Stranik, and Wolfgang Fritzsche. Plasmonic nanoparticle synthesis and bioconjugation for bioanalytical sensing. *Engineering in Life Sciences*, 15(3):266–275, 2015. ISSN 16182863. doi: 10.1002/elsc.201400075.

[17] O. Dial, C. C. Cheng, and A. Scherer. Fabrication of high-density nanostructures by electron beam lithography. *Journal of Vacuum Science and Technology B: Microelectronics and Nanometer Structures*, 16(6):3887–3890, 1998. ISSN 10711023. doi: 10.1116/1.590428.

[18] Ampere A. Tseng, Kuan Chen, Chii D. Chen, and Kung J. Ma. Electron beam lithography in nanoscale fabrication: Recent development. *IEEE Transactions on Electronics Packaging Manufacturing*, 26(2):141–149, 2003. ISSN 1521334X. doi: 10.1109/TEPM.2003.817714.

[19] Frank Burmeister, Claudia Schäfle, Thomas Matthes, Matthias Böhmisch, Johannes Boneberg, and Paul Leiderer. Colloid monolayers as versatile lithographic masks. *Langmuir*, 13(11):2983–2987, 1997. ISSN 07437463. doi: 10.1021/la9621123.

[20] A. Kosiorek, W. Kandulski, P. Chudzinski, K. Kempa, and M. Giersig. Shadow nanosphere lithography: Simulation and experiment. *Nano Letters*, 4(7):1359–1363, 2004. ISSN 15306984. doi: 10.1021/nl049361t.

[21] Christy L. Haynes and Richard P. Van Duyne. Nanosphere lithography: A versatile nanofabrication tool for studies of size-dependent nanoparticle optics. *Journal of Physical Chemistry B*, 105(24):5599–5611, 2001. ISSN 10895647. doi: 10.1021/jp010657m.

[22] Hans Fredriksson, Yury Alaverdyan, Alexandre Dmitriev, Christoph Langhammer, Duncan S. Sutherland, Michael Zäch, and Bengt Kasemo. Hole-mask colloidal lithography. *Advanced Materials*, 19(23):4297–4302, 2007. ISSN 09359648. doi: 10.1002/adma.200700680.

[23] Seung Man Yang, Se Gyu Jang, Dae Geun Choi, Sarah Kim, and Hyung Kyun Yu. Nanomachining by colloidal lithography, 2006. ISSN 16136829.

[24] Stefan A. Maier. *Plasmonics : Fundamentals and Applications*. Springer Science, Business Media LLCSpringer Science, Business Media LLC, 2007. ISBN 9780387331508. doi: 10.1016/j.aca.2010.06.020.

[25] Craig F. Bohren and Donald R. Huffman. *Absorption and Scattering of Light by Small Particles*. Wiley, apr 1998. ISBN 9780471293408. doi: 10.1002/9783527618156.

[26] Michael Quinten. *Optical Properties of Nanoparticle Systems*. Wiley, Weinheim, Germany, jan 2011. ISBN 9783527633135. doi: 10.1002/9783527633135.

[27] Petr Chýlek and Jiyu Zhan. Absorption and scattering of light by small particles. *Applied Optics*, 2009. ISSN 0003-6935. doi: 10.1364/ao.29.003984.

[28] John David Jackson. *Classical Electrodynamics*. Wiley, New York, third edition, 1999. ISBN 047130932X. doi: 10.1119/1.19136.

[29] Geert Verhoeven. Basics of photography for cultural heritage imaging. In Efstratios Stylianidis and Fabio Remondino, editors, *3D Recording, Documentation and Management of Cultural Heritage*, pages 127–251. Whittles Publishing, aug 2016. ISBN 978-184995-168-5.

[30] Robert L. Olmon, Brian Slovick, Timothy W. Johnson, David Shelton, Sang Hyun Oh, Glenn D. Boreman, and Markus B. Raschke. Optical dielectric function of gold. *Physical Review B - Condensed Matter and Materials Physics*, 86(23):1–9, 2012. ISSN 10980121. doi: 10.1103/PhysRevB.86.235147.

[31] P. B. Johnson and R. W. Christy. Optical constants of the noble metals. *Physical Review B*, 6(12):4370–4379, 1972. ISSN 01631829. doi: 10.1103/PhysRevB.6.4370.

[32] Zhuo Li, Liangliang Liu, Hengyi Sun, Yunhe Sun, Changqing Gu, Xinlei Chen, Yun Liu, and Yu Luo. Effective Surface Plasmon Polaritons Induced by Modal Dispersion in a Waveguide. *Physical Review Applied*, 7(4):1–9, 2017. ISSN 23317019. doi: 10.1103/PhysRevApplied.7.044028.

[33] Zhuo Li, Yunhe Sun, Changqing Gu, and Liangliang Liu. Tuning the dispersion of effective surface plasmon polaritons with multilayer systems. *Optics express*, 26(4):4686–4697, 2018. doi: 10.1364/OE.26.004686.

[34] Greg Sun and Jacob B Khurgin. Plasmonic Enhancment of Optical Properties by Isolated and and Coupled Metal Nanoparticles. In *Plasmonics and Plasmonic Metamaterials*, volume Volume 4 of *World Scientific Series in Nanoscience and Nanotechnology*, pages 1–44. World Scientific, dec 2011. ISBN 978-981-4355-27-8. doi: 10.1142/9789814355285_0001.

[35] E. Le Ru and P. Etchegoin. *Principles of Surfance Enhanced Raman Spectroscopy and related plasmonic effets*, volume 1. Elsevier, 2009. ISBN 978-0-444-52779-0. doi: 10.1017/CBO9781107415324.004.

[36] Jorge R. Zurita-Sánchez. Quasi-static electromagnetic fields created by an electric dipole in the vicinity of a dielectric sphere: Method of images. *Revista Mexicana de Fisica*, 55(6):443–449, 2009. ISSN 0035001X.

[37] K. Lance Kelly, Eduardo Coronado, Lin Lin Zhao, and George C. Schatz. The optical properties of metal nanoparticles: The influence of size, shape, and dielectric environment. *Journal of Physical Chemistry B*, 107 (3):668–677, 2003. ISSN 10895647. doi: 10.1021/jp026731y.

[38] Gustav Mie. Beiträge zur Optik trüber Medien, speziell kolloidaler Metallösungen. *Annalen der Physik*, 330(3):377–445, 1908. ISSN 00033804. doi: 10.1002/andp.19083300302.

[39] Qiang Fu and Wenbo Sun. Mie theory for light scattering by a spherical particle in an absorbing medium. *Applied Optics*, 40(9):1354, mar 2001. ISSN 0003-6935. doi: 10.1364/AO.40.001354.

[40] Dimitrios Tzarouchis and Ari Sihvola. Light Scattering by a Dielectric Sphere: Perspectives on the Mie Resonances. *Applied Sciences*, 8(2):184, jan 2018. ISSN 2076-3417. doi: 10.3390/app8020184.

[41] Nader Jalili and Karthik Laxminarayana. A review of atomic force microscopy imaging systems: Application to molecular metrology and biological sciences. *Mechatronics*, 14(8):907–945, 2004. ISSN 09574158. doi: 10.1016/j.mechatronics.2004.04.005.

[42] V.L. Mironov. *Fundamentals of Scanning Probe Microscopy*. NT-MDT, Nizhny Novgorod, 2004. URL `http://ipmras.ru/UserFiles/publications/mironov/Fundamentals_SPM.pdf`.

[43] Pavlo Kliuiev. *Gap modes-coupling of plasmonic nanoparticles with a gold film*. PhD thesis, Friedrich-Schiller-Universität Jena, 2014.

[44] Bruker Corporation. SPM Training Guide, 2010. URL `http://www.nanophys.kth.se/nanophys/facilities/nfl/afm/icon/bruker-help/Content/SPMTrainingGuide/SPMTrainingGuide.htm`.

[45] CC BY-SA 3.0. Diagram illustrating the light path through a dark-field microscope, 2020. URL `https://en.wikipedia.org/wiki/Dark-field_microscopy#/media/File:Dark_Field_Microscope_@D.svg`.

[46] Andreas B Dahlin, Jonas O Tegenfeldt, and Fredrik Höök. Improving the Instrumental Resolution of Sensors Based on Localized Surface Plasmon Resonance. *Analytical Chemistry*, 78(13):4416–4423, jul 2006. ISSN 0003-2700. doi: 10.1021/ac0601967.

[47] E. Kretschmann. The ATR method with focused light - Application to guided waves on a grating. *Optics Communications*, 26(1):41–44, 1978. ISSN 00304018. doi: 10.1016/0030-4018(78)90337-1.

[48] S .J. Randolph, J .D. Fowlkes, and P .D. Rack. Focused, Nanoscale Electron-Beam-Induced Deposition and Etching. *Critical Reviews in Solid State and Materials Sciences*, 31(3):55–89, sep 2006. ISSN 1040-8436. doi: 10.1080/10408430600930438.

[49] Stephen Y Chou. Nanoimprint lithography. *Journal of Vacuum Science & Technology B: Microelectronics and Nanometer Structures*, 14(6):4129, nov 1996. ISSN 0734211X. doi: 10.1116/1.588605.

[50] L. J. Guo. Nanoimprint Lithography: Methods and Material Requirements. *Advanced Materials*, 19(4):495–513, feb 2007. ISSN 09359648. doi: 10.1002/adma.200600882.

[51] Andrea Csáki, Ondrej Stranik, and Wolfgang Fritzsche. Localized surface plasmon resonance based biosensing. *Expert Review of Molecular Diagnostics*, 18(3):279–296, mar 2018. ISSN 1473-7159. doi: 10.1080/14737159.2018.1440208. URL `https://doi.org/10.1080/14737159.2018.1440208`.

[52] Burcu Ögüt, Ralf Vogelgesang, Wilfried Sigle, Nahid Talebi, Christoph T Koch, and Peter A van Aken. Hybridized Metal Slit Eigenmodes as an Illustration of Babinet's Principle. *ACS Nano*, 5(8):6701–6706, aug 2011. ISSN 1936-0851. doi: 10.1021/nn2022414.

[53] Svetlana Syrenova, Carl Wadell, and Christoph Langhammer. Shrinking-Hole Colloidal Lithography: Self-Aligned Nanofabrication of Complex Plasmonic Nanoantennas. *Nano Letters*, 14(5):2655–2663, may 2014. ISSN 1530-6984. doi: 10.1021/nl500514y.

[54] V. Bouchiat and D. Esteve. Lift-off lithography using an atomic force microscope. *Applied Physics Letters*, 69(20):3098–3100, 1996. ISSN 00036951. doi: 10.1063/1.117317.

[55] Richard D. Piner, Jin Zhu, Feng Xu, Jiří Homola, and Chad A. Mirkin. 'Dip-pen' nanolithography. *Science*, 283(5402):661–663, 1999. ISSN 00368075. doi: 10.1126/science.283.5402.661.

[56] L. L. Sohn and R. L. Willett. Fabrication of nanostructures using atomic-force-microscope-based lithography. *Applied Physics Letters*, 67(11): 1552–1554, 1995. ISSN 00036951. doi: 10.1063/1.114731.

[57] Pavla Beresova, Ondrej Stranik, and Ladislav Kalvoda. Colloidal (-less) based lithography methods for fabrication of plasmonic nanostructures. In *Molecular plasmonics poster session*, Jena, Germany, 2019.

[58] Angelina Pittner, Sebastian Wendt, David Zopf, André Dathe, Norman Grosse, Andrea Csáki, Wolfgang Fritzsche, and Ondrej Stranik. Fabrication of micro-patterned substrates for plasmonic sensing by piezo-dispensing of colloidal nanoparticles. *Analytical and Bioanalytical Chemistry*, 411(8):1537–1547, 2019. ISSN 1618-2650. doi: 10.1007/s00216-019-01587-7.

[59] Thomas R.M. Barends, Lutz Foucar, Albert Ardevol, Karol Nass, Andrew Aquila, Sabine Botha, R. Bruce Doak, Konstantin Falahati, Elisabeth Hartmann, Mario Hilpert, Marcel Heinz, Matthias C. Hoffmann, Jürgen Köfinger, Jason E. Koglin, Gabriela Kovacsova, Mengning Liang, Despina Milathianaki, Henrik T. Lemke, Jochen Reinstein, Christopher M. Roome, Robert L. Shoeman, Garth J. Williams, Irene Burghardt, Gerhard Hummer, Sébastien Boutet, and Ilme Schlichting. Direct observation of ultrafast collective motions in CO myoglobin upon ligand dissociation. *Science*, 350(6259):445–450, 2015. ISSN 10959203. doi: 10.1126/science.aac5492.

[60] Mike Boland, Lovedeep Kaur, Feng Ming Chian, and Thierry Astruc. Muscle Proteins. In Laurence Melton, Fereidoon Shahidi, and Peter B T Encyclopedia of Food Chemistry Varelis, editors, *Encyclopedia of Food Chemistry*, pages 164–179. Elsevier, Oxford, 2019. ISBN 978-0-12-814045-1. doi: 10.1016/B978-0-08-100596-5.21602-8.

[61] Gary P Roberts, Hwan Youn, and Robert L Kerby. CO-sensing mechanisms. *Microbiology and molecular biology reviews : MMBR*, 68(3):453–473, sep 2004. ISSN 1092-2172. doi: 10.1128/MMBR.68.3.453-473.2004.

[62] K Chu, J Vojtchovsky, B H McMahon, R M Sweet, J Berendzen, and I Schlichting. Structure of a ligand-binding intermediate in wild-type carbonmonoxy myoglobin. *Nature*, 403(6772):921–923, feb 2000. ISSN 0028-0836 (Print). doi: 10.1038/35002641.

[63] Eric Oldfield, Kermin Guo, Joseph D Augspurger, and Clifford E Dykstra. A molecular model for the major conformational substates in heme proteins. *Journal of the American Chemical Society*, 113(20):7537–7541, sep 1991. ISSN 0002-7863. doi: 10.1021/ja00020a014.

[64] R Elber and M Karplus. Multiple conformational states of proteins: a molecular dynamics analysis of myoglobin. *Science*, 235(4786):318–321, jan 1987. ISSN 0036-8075. doi: 10.1126/science.3798113.

[65] Joan S Valentine, Robert P Sheridan, Leland C Allen, and Peter C Kahn. Coupling between oxidation state and hydrogen bond conformation in heme proteins. *Proceedings of the National Academy of Sciences*, 76(3): 1009–1013, mar 1979. ISSN 0027-8424. doi: 10.1073/pnas.76.3.1009.

[66] Silje Ottestad, Oddvin Sørheim, Karsten Heia, Josefine Skaret, and Jens Petter Wold. Effects of storage atmosphere and heme state on the color and visible reflectance spectra of salmon (Salmo salar) fillets. *Journal of Agricultural and Food Chemistry*, 59(14):7825–7831, 2011. ISSN 00218561. doi: 10.1021/jf201150x.

[67] Zhimin Tao, Jerry Goodisman, and Abdul-Kader Souid. Oxygen Measurement via Phosphorescence: Reaction of Sodium Dithionite with Dissolved Oxygen. *The Journal of Physical Chemistry A*, 112(7):1511–1518, feb 2008. ISSN 1089-5639. doi: 10.1021/jp710176z.

[68] Lynn D Robertson and David Roper. Laboratory Methods Used in the Investigation of the Haemolytic Anaemias. In Barbara J Bain, Imelda Bates, Michael A B T Dacie Laffan, and Lewis Practical Haematology (Twelfth Edition), editors, *Dacie and Lewis Practical Haematology*, pages 214–227. Elsevier, 2017. ISBN 978-0-7020-6696-2. doi: 10.1016/B978-0-7020-6696-2.00011-4.

[69] Dileep Mampallil and Huseyin Burak Eral. A review on suppression and utilization of the coffee-ring effect. *Advances in Colloid and Interface Science*, 2018. ISSN 00018686. doi: 10.1016/j.cis.2017.12.008.

[70] David Nečas and Petr Klapetek. Gwyddion: an open-source software for SPM data analysis. *Open Physics*, 10(1):181–188, jan 2012. ISSN 2391-5471. doi: 10.2478/s11534-011-0096-2.

[71] Kazuyoshi Kurihara, Kaori Nakamura, and Koji Suzuki. Asymmetric SPR sensor response curve-fitting equation for the accurate determination of SPR resonance angle. *Sensors and Actuators, B: Chemical*, 86(1): 49–57, 2002. ISSN 09254005. doi: 10.1016/S0925-4005(02)00146-6.

[72] Ravi Kant. Surface plasmon resonance based fiber–optic nanosensor for the pesticide fenitrothion utilizing Ta2O5 nanostructures sequestered onto a reduced graphene oxide matrix. *Microchimica Acta*, 187(1):1–11, 2020. ISSN 14365073. doi: 10.1007/s00604-019-4002-8.

[73] Christoph Lemke, Till Leißner, Alwin Klick, Jacek Fiutowski, Jörn Willers Radke, Martin Thomaschewski, Jakob Kjelstrup-Hansen, Horst Günter Rubahn, and Michael Bauer. The complex dispersion relation of surface plasmon polaritons at gold/para-hexaphenylene interfaces. *Applied Physics B: Lasers and Optics*, 116(3):585–591, 2014. ISSN 09462171. doi: 10.1007/s00340-013-5737-2.

[74] Matts Björck and Gabriella Andersson. GenX : an extensible X-ray reflectivity refinement program utilizing differential evolution. *Journal of Applied Crystallography*, 40(6):1174–1178, dec 2007. ISSN 0021-8898. doi: 10.1107/S0021889807045086.

[75] Miho Yasaka. X-ray thin-film measurement techniques V. X-ray reflectivity measurement. *The Rigaku Journal*, 26(2):1–9, 2010. ISSN 2187-9974.

[76] Briliant Adhi Prabowo, Agnes Purwidyantri, and Kou-Chen Liu. Surface Plasmon Resonance Optical Sensor: A Review on Light Source Technology. *Biosensors*, 8(3):80, aug 2018. ISSN 2079-6374. doi: 10.3390/bios8030080.

[77] Panu Artimo, Manohar Jonnalagedda, Konstantin Arnold, Delphine Baratin, Gabor Csardi, Edouard de Castro, Séverine Duvaud, Volker Flegel, Arnaud Fortier, Elisabeth Gasteiger, Aurélien Grosdidier, Céline Hernandez, Vassilios Ioannidis, Dmitry Kuznetsov, Robin Liechti, Sébastien Moretti, Khaled Mostaguir, Nicole Redaschi, Grégoire Rossier, Ioannis Xenarios, and Heinz Stockinger. ExPASy: SIB bioinformatics resource portal. *Nucleic Acids Research*, 40(W1):W597–W603, may 2012. ISSN 0305-1048. doi: 10.1093/nar/gks400.

[78] The UniProt Consortium. UniProt: a worldwide hub of protein knowledge. *Nucleic Acids Research*, 47(D1):D506–D515, nov 2018. ISSN 0305-1048. doi: 10.1093/nar/gky1049.